The Astrophysical Journal Supplement Series, 189:156–180, 2010 July doi:10.1088/0067-0049/189/1/156
© 2010. The American Astronomical Society. All rights reserved. Printed in the U.S.A.

THEORY OF DISPERSED FIXED-DELAY INTERFEROMETRY FOR RADIAL VELOCITY EXOPLANET SEARCHES

Julian C. van Eyken[1,2,5], Jian Ge[1,5], and Suvrath Mahadevan[1,3,4,5]
[1] Department of Astronomy, University of Florida, 211 Bryant Space Science Center, P.O. Box 112055, Gainesville, FL 32611-2055, USA; vaneyken@ipac.caltech.edu, jge@astro.ufl.edu, suvrath@astro.psu.edu
[2] NASA Exoplanet Science Institute, California Institute of Technology, 770 South Wilson Avenue, M/S 100-22, Pasadena, CA 91125, USA
[3] Department of Astronomy & Astrophysics, The Pennsylvania State University, University Park, PA 16802, USA
[4] Center for Exoplanets and Habitable Worlds, The Pennsylvania State University, University Park, PA 16802, USA
Received 2009 July 3; accepted 2010 May 28; published 2010 June 28

ABSTRACT

The dispersed fixed-delay interferometer (DFDI) represents a new instrument concept for high-precision radial velocity (RV) surveys for extrasolar planets. A combination of a Michelson interferometer and a medium-resolution spectrograph, it has the potential for performing multi-object surveys, where most previous RV techniques have been limited to observing only one target at a time. Because of the large sample of extrasolar planets needed to better understand planetary formation, evolution, and prevalence, this new technique represents a logical next step in instrumentation for RV extrasolar planet searches, and has been proven with the single-object Exoplanet Tracker (ET) at Kitt Peak National Observatory, and the multi-object W. M. Keck/MARVELS Exoplanet Tracker at Apache Point Observatory. The development of the ET instruments has necessitated fleshing out a detailed understanding of the physical principles of the DFDI technique. Here we summarize the fundamental theoretical material needed to understand the technique and provide an overview of the physics underlying the instrument's working. We also derive some useful analytical formulae that can be used to estimate the level of various sources of error generic to the technique, such as photon shot noise when using a fiducial reference spectrum, contamination by secondary spectra (e.g., crowded sources, spectroscopic binaries, or moonlight contamination), residual interferometer comb, and reference cross-talk error. Following this, we show that the use of a traditional gas absorption fiducial reference with a DFDI can incur significant systematic errors that must be taken into account at the precision levels required to detect extrasolar planets.

Key words: instrumentation: interferometers – instrumentation: spectrographs – methods: analytical – planetary systems – techniques: radial velocities

Online-only material: color figures

1. THE DFDI CONCEPT AND THE ET PROGRAM

1.1. The Need for a New Instrument

Despite the remarkable achievements in extrasolar planet detection over the last decade, identification of many more planets is still needed to constrain formation and evolutionary models. This is partially because of the unexpected diversity of planet properties uncovered, and partially because of a lack of large, well-defined, unbiased target search lists—the primary concern naturally having been to find planets in the first place. To this point many surveys have been subject to completeness issues or in some cases deliberate biases toward planet detection (e.g., da Silva et al. 2006), making it difficult to perform robust statistical analyses of the known planet sample. Armitage (2007) concluded that there is still a strong need for large uniform surveys to enlarge the statistical sample available: drawing on the unbiased survey of Fischer & Valenti (2005), he was only able to find a uniform subsample of 22 of the over 170 planets then known that satisfied the requirements for a statistical comparison with models.

A few thousand stars have been searched between the various RV surveys since the first RV discoveries of giant extrasolar planets around solar-type stars (Mayor & Queloz 1995), including a large fraction of the late-type, stable stars down to visual magnitude ∼8. Improved instrument light throughput would help facilitate the survey of fainter stars. (A review of radial velocity (RV) discoveries is given by Udry et al. 2007.) Although the rate of detections from transit surveys will likely increase, transit surveys can only detect the small fraction of planets which happen to eclipse their parent stars (∼10% probability for hot Jupiters, from geometrical considerations— Kane et al. 2004). Furthermore, the complementary information gained from RV detections remains of great value. There is therefore a strong case for finding a technique capable of RV surveys down to faint magnitudes and at faster speeds than have been achieved over the last decade. The Exoplanet Tracker (ET) instruments are a new type of fiber-fed RV instrument based on the "dispersed fixed-delay interferometer" (DFDI), built with the goal of satisfying this requirement.

1.2. The DFDI Principle

The RV technique for detecting exoplanets consists in measuring the reflex motion of the parent star due to an orbiting planet by measuring very precisely the resulting Doppler shifts of the stellar absorption lines. Achieving this requires extremely high precision: internal precisions now typically reach down to the 3 m s^{-1} level (Butler et al. 1996; Vogt et al. 2000), and even as low as 1 m s^{-1} or better (Pepe et al. 2005). For comparison, a Jupiter analog in a circular orbit around a solar-type

[5] Visiting Astronomers, Kitt Peak National Observatory, National Optical Astronomy Observatory, which is operated by the Association of Universities for Research in Astronomy, Inc. (AURA), under cooperative agreement with the National Science Foundation.

star would cause sinusoidal RV variations with an amplitude of about 12.5 m s^{-1}. Exoplanet RV surveys have traditionally depended on recording very high resolution echelle spectra, either cross-correlating the spectra with reference template spectra, or fitting functions to the line profiles themselves to measure the positions of the centroids.

The DFDI technique, upon which the ET instruments are based, comprises a Michelson interferometer followed by a low- or medium-resolution post-disperser (also referred to by Erskine 2003 as an externally dispersed interferometer, or "EDI," emphasizing the distinction from techniques where the dispersing element is internal to the interferometer). The effective resolution of the instrument is primarily determined by the interferometer, so the post-dispersing spectrograph can be of much lower resolution than in traditional dispersive techniques, and consequently can be smaller, cheaper, and have higher throughput (Ge 2002; Ge et al. 2003a, 2003b). The technique is closely related to Fourier transform spectroscopy: the post-disperser effectively creates a continuum of very narrow bandpasses for the interferometer, increasing the interference fringe contrast. All of the information needed is contained in the fringe phase and visibility. It emerges that since we are only interested in the Doppler shift of the lines, measurements are required at essentially only one value of interferometer delay (hence "fixed delay").

The cost of the instrument is comparatively low, and most importantly, it can operate in a single-order mode: where traditional echelle spectrograph techniques operate by spreading a single stellar spectrum over an entire CCD detector in multiple orders, here the spectrum only takes up one strip along the detector. Spectra from multiple stars can therefore be lined up at once on a single detector. In combination with a wide-field multi-fiber telescope, this makes multi-object RV planet surveying possible (Ge 2002; Ge et al. 2002; Mahadevan et al. 2003). The multi-object Keck ET instrument based on the DFDI technique is one of the first instruments to be built with this purpose (Ge et al. 2009).[6]

The very high levels of precision required for planet detection and the difficulty of directly measuring absolute wavelengths mean that some kind of stationary reference spectrum is invariably used as a calibration. Various types of fiducial reference have been employed to overcome these problems (e.g., Griffin & Griffin 1973; Campbell & Walker 1979), but the references of choice have generally become ThAr emission lamps (Baranne et al. 1996) and iodine vapor absorption cells placed within the optical beam path (Butler et al. 1996). In this respect, the ET instruments are the same, and we discuss the use of such references with the DFDI technique in this paper.

1.3. A Brief History

The idea of using the combination of a Michelson interferometer with a post-disperser was first proposed for precision Doppler planet searches by D. J. Erskine in 1997, at Lawrence Livermore National Laboratory (Erskine & Ge 2000; Ge 2002; Ge et al. 2002; Erskine 2003). The same approach is being followed by Edelstein et al. (2006) in the infrared, in an attempt to find planets around late-type stars. A similar approach is discussed by Mosser et al. (2003) for asteroseismology and the measurement of stellar oscillations; more recently the technique has also been adopted for the USNO Dispersed Fourier Transform Spectrograph (dFTS) instrument (Hajian et al. 2007; Behr et al. 2009; in this last case, the interferometer delay is also varied so that high-resolution spectra can be reconstructed in addition to extracting Doppler shift information—see also Erskine & Edelstein 2004).

The idea of dispersed interferometry itself is by no means new: Michelson himself recognized the use of interferometers for spectroscopy (Michelson 1903), and even proposed combining a disperser in series with a Michelson interferometer. In this case the disperser, a prism, was placed *before* the interferometer, allowing only a narrow bandwidth of light to enter the interferometer in the first place. In what was likely the first realization of a DFDI, Edser & Butler (1898) placed a Fabry–Perot type interferometer in front of a spectrograph[7] to produce dispersed fringes (effectively an interferometer comb—see Section 2.4), which they used as a fiducial reference for measuring the wavelengths of spectral lines. Such dispersed fringes were later to become known as "Edser–Butler fringes" (Lawson 2000).

Somewhat later, along with the development of P. Connes' spectromètre interférentiel à sélection par l'amplitude de modulation (SISAM; described in Jacquinot 1960), various combinations of interferometers with dispersers began to be seen in the field of astronomy. Examples include Geake et al. (1959), using a Fabry–Perot in front of a spectrograph to increase throughput; and the later spatial heterodyne spectroscopy (SHS; Harlander et al. 1992) and heterodyned holographic spectroscopy (HHS; Frandsen et al. 1993; Douglas 1997) techniques, using *internally* dispersed interferometers, where the interferometer mirrors were replaced with gratings. Barker & Hollenbach (1972) outlined an early example of the use of true fixed-delay interferometry for velocimetry, measuring the velocities of laser-illuminated projectiles in the laboratory. The use of a Michelson interferometer for actual astronomical RV measurements was proposed shortly afterward by Gorskii & Lebedev (1977) and Beckers & Brown (1978). Forrest & Ring (1978) also proposed using a Michelson interferometer with a fixed delay for high-precision Doppler measurements of single spectral lines for the detection of stellar oscillations, and more recent examples of similar spectroscopic techniques include Connes (1985) and McMillan et al. (1993, 1994). Others have also used similar techniques for Doppler *imaging* over very narrow bandpasses, notably the wide-angle Doppler imaging interferometer (WAMDII) and Global Oscillation Network Group (GONG) projects (Shepherd et al. 1985; Harvey & The GONG Instrument Team 1995).

Many of these interferometric instruments, however, suffered from the limitation of having an extremely narrow bandpass, tending to limit their application to only bright targets. The DFDI technique used in the ET instruments allows for an arbitrarily wide bandpass, limited only by the spectrograph capabilities, while still retaining the high-resolution spectral information needed for precision velocity measurements. The first such DFDI instruments were built at the Lawrence Livermore National Laboratory and the Lick 1 m telescope between 1997 and 1999, and were reported in Erskine & Ge (2000) and Ge et al. (2002). The ET project was undertaken shortly after.

[6] Comparable traditional dispersive multi-object instruments are the VLT GIRAFFE and UVES/FLAMES spectrographs (Loeillet et al. 2008), and the MMT Hectochelle (Szentgyorgyi & Furész 2007).

[7] It was mistakenly stated in van Eyken et al. (2004a) that Edser & Butler (1898) used a Michelson rather than a Fabry–Perot interferometer, which has certain disadvantages in this application (D. J. Erskine 2005, private communication).

1.4. The ET Project

The ET project began at Penn State University in 2000, continuing at the University of Florida from 2004. Early lab tests were performed at Penn State, and prototype test runs were conducted at the McDonald Observatory Hobby-Eberly Telescope in late 2001, and at the Palomar 200 inch telescope in early 2002 (Ge et al. 2003b; Mahadevan 2006).

Two ET instruments have now been built: the single-object prototype ET (van Eyken et al. 2004b; Mahadevan et al. 2008a), permanently installed at the KPNO 2.1 m telescope in 2003 after a temporary test run in 2002 August; and the multi-object Keck ET, first installed at the APO Sloan 2.5 m telescope in 2005 March, upgraded and moved to a more stable location at the same telescope later that year, and then further upgraded and fully installed as facility instrument housed in its own custom-built room in 2008 September. The latter instrument will function as the workhorse for the SDSS-III "Multi-object APO Radial Velocity Exoplanet Large-area Survey" (MARVELS; Ge et al. 2009).

Proof of concept was achieved using the KPNO ET with the first DFDI planet detection, a confirmation of the known companion to 51 Pegasi (van Eyken et al. 2004a). Our first planet discovery, HD 102195b (ET-1), was also later made using this instrument (Ge et al. 2006). The multi-object Keck ET is a full scale instrument developed to satisfy the survey requirements laid out in Section 1.1, and it is anticipated that it will be able to make a significant contribution to the field of extrasolar planet searches over the next decade (Ge et al. 2009).

2. INSTRUMENT PRINCIPLES AND THEORY

Although various forms of the DFDI have been employed before, the concept, particularly in its specific application to exoplanet finding, is rather new. Much of the work in understanding the data from the instrument has therefore involved coming to a full understanding of the physics of the instrument itself. Related theory is discussed in a number of sources (for example, Goodman 1985; Erskine & Ge 2000; Lawson 2000; Ge 2002; Ge et al. 2002; Erskine 2003; Mosser et al. 2003; van Eyken et al. 2003); an attempt is made here to draw together, expand on, and precisely state the theoretical material needed for a complete understanding of the instrument, and to provide an overview of the physics underlying the instrument's working from the perspective of precision RV planet detection. The approach taken here allows for some important insights, particularly regarding certain errors arising from the use of a common-path fiducial reference spectrum such as that from an iodine gas absorption cell. In addition, we derive in Section 3 some useful general formulae that can be applied to estimate analytically the magnitude of both these and a number of other types of error generic to the technique.

Taken together, this discussion should provide some of the fundamentals necessary for understanding and interpreting DFDI data. Appendix B gives a derivation showing the relation to the approach employed by Erskine (2003), to which the approach here is complementary.

2.1. Formation of a Fringing Spectrum

Figure 1 shows a highly simplified schematic of a DFDI, consisting of the two main components, a fiber-fed Michelson interferometer and a disperser, followed by a detector. Light input from the fiber is split into two paths along the arms of the interferometer and then recombined at the beamsplitter. The output is fed to the disperser, represented for convenience as a prism, though generally this will be a spectrograph. An etalon is placed in one of the interferometer arms to create a fixed optical path difference (or "delay"), $d = d_0$, between the two arms, while allowing for adequate field widening (Hilliard & Shepherd 1966; Mahadevan et al. 2008a). d_0 is typically on the order of millimeters. In practice, an iodine vapor cell can also be placed in the optical path before or after the interferometer to act as a fiducial reference (Section 2.6).

Inputting a wide collimated beam of monochromatic light into the instrument with both interferometer mirrors exactly perpendicular to the light travel path will give either a bright or a dark fringe at the output of the interferometer (Figure 1(A)), depending on whether the exact path difference d between the two arms corresponds to constructive or destructive interference. If we were to scan one of the mirrors back and forth, the flux at the interferometer output would vary sinusoidally as a function of d. If we now tilt this mirror along the axis in the plane of the page, we effectively scan a small range of delays along the y-direction (i.e., perpendicular to the axis of the tilt and in the plane of the mirror, corresponding to the slit direction in the spectrograph). Hence we would see a series of parallel bright and dark fringes, now varying sinusoidally as a function of y.[8]

Consider first a very high (actually infinite) resolution spectrograph disperser for the sake of argument: following the beam through until it reaches the detector plane would result in a single emission line with fringes along the slit direction, as shown in Figure 1(C). Switching the input spectrum to white light, which can be thought of as a continuum of neighboring delta functions in wavelength (λ) space, leads to a similar fringe pattern on the detector at every wavelength channel. Due to the fact that, in terms of the number of wavelengths, the optical path difference is different for different wavelengths, each fringe is slightly offset in phase from its neighbors (and very slightly different in period). This gives rise to the series of parallel lines known as the interferometer "comb," shown in Figure 1(D). Going further and inputting a stellar spectrum into the instrument would simply give the product of the stellar spectrum and the comb, as in Figure 1(E). Finally, changing to the real case of a low- or medium-resolution spectrograph as for an ET-type instrument, the comb is no longer (or barely) resolved, and we see a spectrum like that in Figure 1(F). Such a spectrum is sometimes referred to as a spectrum "channeled with fringes," also known as Edser–Butler fringes (Edser & Butler 1898; Lawson 2000; Ge 2002). The remaining fringes contain high spatial frequency Doppler information that has been heterodyned down to lower spatial frequencies by the interferometer comb (Erskine 2003; Mahadevan 2006). It is this heterodyning that allows for the use of a low-resolution spectrograph at low dispersion, and is the key to the DFDI technique.

2.2. Fringe Phase and Visibility

Above we outlined a simple intuitive way of understanding the formation of the DFDI fringing spectrum. For a full mathematical description, we proceed by a slightly different route. Each wavelength channel on the detector has an associated sinusoidal fringe running along the slit direction, where by "channel," we mean specifically an infinitesimally wide strip

[8] Another way of sampling the fringes is to scan the interferometer delay in very small steps (see Erskine 2003): this allows for certain advantages in calibration as well as a one-dimensional spectrum which requires less detector real estate, but comes at the disadvantage of requiring an actively controlled interferometer. The principles are the same, however.

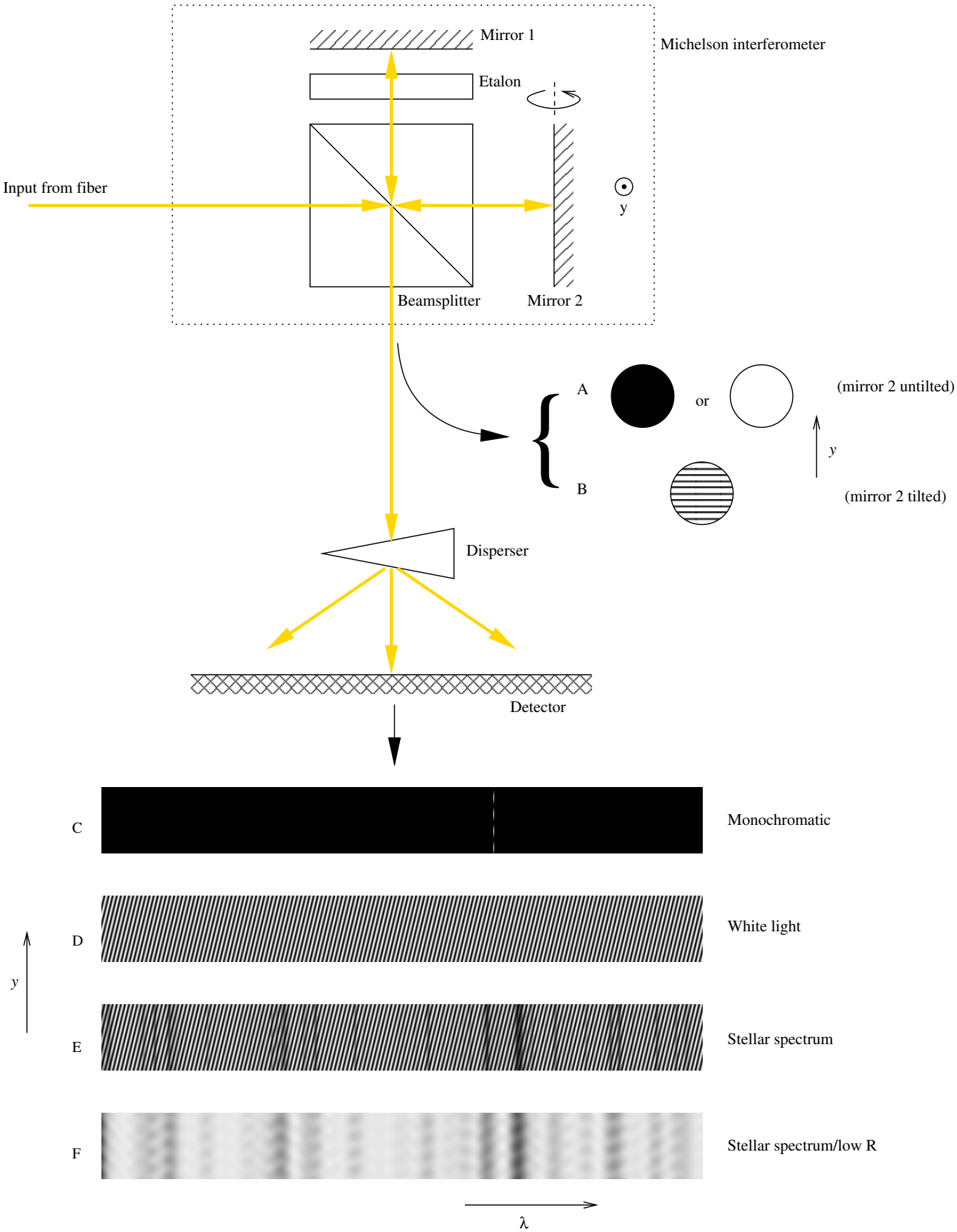

Figure 1. Dispersed interferometer schematic. *y* corresponds to position in the slit direction (directed out of the page in the interferometer schematic), and λ indicates wavelength in the dispersion direction. (A) Output from interferometer alone with monochromatic light input, and mirror 2 untilted. (B) The same with mirror 2 tilted along the axis in the plane of the page, as shown. (C) Image on detector with monochromatic light at very high resolution. One fringed emission line is seen. (D) Detector image with white light input. (E) Image with stellar spectrum input. (F) As for E but at low resolution.

(A color version of this figure is available in the online journal.)

of the spectrum along the slit direction at pixel position j, where j need not necessarily be an integer. A given fringe has an associated phase and visibility, where visibility is a measure of the contrast in the fringe, defined as the ratio of the amplitude of the fringe to its central (mean) flux value. Equivalently, this can be stated as $(I_{\max} - I_{\min})/(I_{\max} + I_{\min})$, where $I_{\max}$ and $I_{\min}$ are the maximum and minimum flux values in the fringe (Michelson 1903). Here we introduce the concept of a "whirl" (Erskine & Ge 2000): the phase and visibility for a fringe can together be thought of as representing a vector, with the visibility representing the magnitude. These quantities can be determined in a number of ways; in general we simply fit a sinusoid. An ensemble of such vectors representing a full spectrum of channels is called a whirl. The whirl is the directly measured quantity from a fringing spectrum and contains the information relevant to velocity determination. Vector operations such as addition, subtraction, and scalar products can be performed on these whirls just as for the individual vectors (Erskine & Ge 2000).

To understand what determines the values of the phase and visibility for a fringe, we can consider the contribution from each wavelength of light to a particular channel on the detector (remembering that although the channel is infinitesimally wide in its spacial extent in the dispersion direction, it still has a finite bandwidth). Each contributing wavelength has passed through the interferometer, and for an ideal interferometer, it will contribute a sinusoid of 100% visibility like that in Figure 1(C). The flux of these sinusoids on the detector can each be described by $\Re\{1 + \exp(\mathrm{i}2\pi d/\lambda)\}$, where d varies linearly with position y along the length of the slit, and $\Re\{\ldots\}$ represents the real part of a complex expression. Since the spectrograph has finite resolution, a narrow band of such wavelengths will contribute to any given channel, owing to the overlap of line spread functions (LSFs) from neighboring wavelengths. The measured fringe along the slit direction is a continuous summation of those sinusoids, weighted by the flux of the spectrum contributing to that channel, $Q_j(\lambda)$, where Q is given by the product of the power spectrum coming into the instrument and the spectrograph response function at that channel on the detector. We use the term "spectrograph response function" throughout to refer to the light throughput as a function of wavelength at a given infinitesimal point on the detector, or equivalently, at a given channel in the image on the detector. (This is distinct from, though closely related to, the LSF—see Appendix A.)

Switching from wavelength to wavenumber $\kappa \equiv 1/\lambda$, and dropping the j subscript for simplicity, the summation of sinusoids can be expressed as

$$\begin{aligned} I(d) &= \int Q(\kappa)\,\Re\{1 + e^{i2\pi\kappa d}\}\,d\kappa \\ &= \int Q(\kappa)\,d\kappa + \Re\left\{\int Q(\kappa) e^{i2\pi\kappa d}\,d\kappa\right\}, \end{aligned} \tag{1}$$

where $I(d)$ is the measured flux along the slit direction. The first term on the right-hand side is simply the total integrated flux in the channel, which must be real valued. The second term can immediately be identified as the real part of a Fourier transform, $\Re\{\mathcal{F}[Q]_d\}$, with delay as the conjugate variable to wavenumber, and shows the close relationship between DFDI instruments and Fourier transform spectroscopy (Jacquinot 1960).

Normalizing by dividing through by the total flux, we can define the complex quantity $\boldsymbol{\alpha}$ such that

$$I_{\mathrm{norm}}(d) = 1 + \Re\left\{\frac{\mathcal{F}[Q(\kappa)]_d}{\int Q(\kappa)\,d\kappa}\right\} = 1 + \Re\{\boldsymbol{\alpha}\}, \tag{2}$$

where

$$\boldsymbol{\alpha} \equiv \alpha e^{i\phi_\alpha} \equiv \frac{\mathcal{F}[Q(\kappa)]_d}{\int Q(\kappa)\,d\kappa}. \tag{3}$$

This is the fundamental equation for DFDI fringe formation: the quantity $\boldsymbol{\alpha}$ is the "complex degree of coherence" (Goodman 1985), and describes the phase, ϕ_α, and amplitude, α, of the normalized fringes (i.e., the visibility), as a function of d and the input spectrum. $\boldsymbol{\alpha}$ is referred to here as the *complex visibility.*[9] More rigorous derivations of this can be found in Goodman (1985, chap. 5) and Lawson (2000), but this explanation is adequate for our purposes.

In order to understand the actual form of the fringes seen in a DFDI, it is important to realize that the portion of spectrum contributing to any given channel, Q, has a very narrow passband (for the ET instruments, $\Delta\lambda/\lambda \sim 1$ Å/5000 Å $= 2 \times 10^{-4}$). We imagine Q as being a shifted version of a function Q_0, where Q_0 has a characteristic width $\Delta\kappa$ and is centered at zero wavenumber. We shift Q_0 in wavenumber so that its center falls at wavenumber $\kappa = \overline{\kappa}$, and we have $Q(\kappa) = Q_0(\kappa - \overline{\kappa})$. By the Fourier shift theorem we can write

$$\mathcal{F}[Q]_d = \mathcal{F}[Q_0(\kappa - \overline{\kappa})]_d = e^{-i2\pi d\overline{\kappa}}\mathcal{F}[Q_0]_d. \tag{4}$$

The right-hand side shows two components. The exponential term represents a linear phase variation with delay, varying on the scale of the period $1/\overline{\kappa}$. The second term, the Fourier transform, represents a modulation of this signal. By the reciprocal scaling property of Fourier transforms, the second term can be expected to vary on minimum length scales of the order of the reciprocal of the width of Q_0, that is, on scales of $1/\Delta\kappa$. Since $1/\Delta\kappa \gg 1/\overline{\kappa}$, Equation (4) represents a sinusoidal fringe of frequency $\overline{\kappa}$ modulated by a slow variation in both phase and amplitude. To see this more clearly, we can substitute Equation (4) into the first expression on the right-hand side of Equation (2) and write

$$I_{\mathrm{norm}}(d) = 1 + \frac{\Re\{e^{-i2\pi d\overline{\kappa}}\mathcal{F}[Q_0]_d\}}{\int Q(\kappa)\,d\kappa}. \tag{5}$$

If we define

$$\boldsymbol{\alpha}_0(d) \equiv \alpha_0(d)e^{i\phi_{\alpha_0}(d)} \equiv \frac{\mathcal{F}[Q_0]_d}{\int Q(\kappa)\,d\kappa}, \tag{6}$$

we can rewrite Equation (5) as

$$\begin{aligned} I_{\mathrm{norm}}(d) &= 1 + \Re\{\boldsymbol{\alpha}_0(d)e^{-i2\pi d\overline{\kappa}}\} \\ &= 1 + \alpha_0(d)\cos(2\pi d\overline{\kappa} - \phi_{\alpha_0}(d)) \end{aligned} \tag{7}$$

(where we have simplified the negative in the cosine term using the symmetry of the cosine function). This clearly shows the form of the fringe. Over large ranges of d, the fringe appears like a "carrier wave," given by the cosine term, that is slowly modulated in phase and amplitude by an envelope $\boldsymbol{\alpha}_0$ (the "coherence envelope," Lawson 2000). Over the length of the

[9] The quantity is generally represented by the letter $\boldsymbol{\gamma}$ in the literature cited. We use $\boldsymbol{\alpha}$ here instead purely for clearer distinction between bold-faced vector and regular-faced amplitude representations.

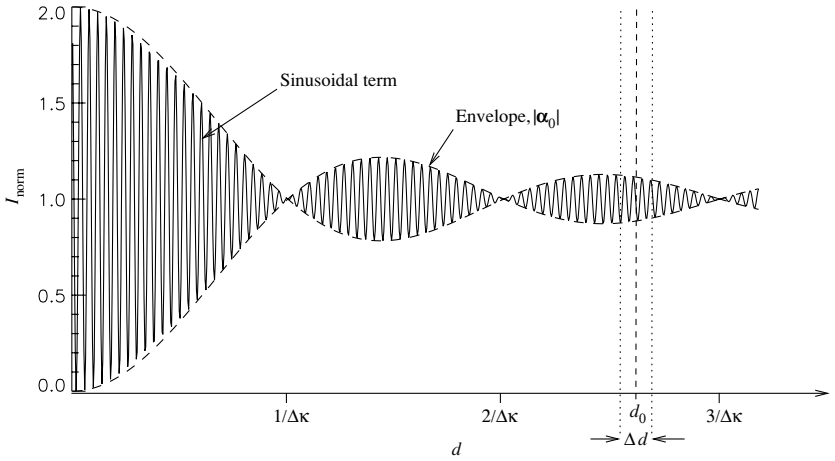

Figure 2. Interferogram showing the coherence envelope due to a rectangular bandpass modulating the sinusoidal fringe. Along the slit direction of a fringing spectrum, a very small part of the interferogram is sampled over the range $d_0 \pm \Delta d/2$.

slit direction on the detector, we sample only a very small range of delays, $d_0 - \Delta d/2 \leqslant d \leqslant d_0 + \Delta d/2$, where d_0 is determined by the interferometer etalon, as before, and Δd is typically a few wavelengths. Over this range, the variation in $\boldsymbol{\alpha}_0$ is small as we show below, so we see only an approximately uniform sinusoid (see Figure 2) along a single wavelength channel on the detector. In measuring the phase and visibility of this fringe, we essentially make a measurement of $\boldsymbol{\alpha}_0$ at the fixed delay $d = d_0$. The phase offset of the sinusoid is determined by the argument of $\boldsymbol{\alpha}_0$, ϕ_{α_0}. The measured (absolute) fringe visibility is simply the amplitude of the normalized fringe, α_0.

In general, we can estimate a rough order of magnitude for the fractional change in the magnitude of the visibility between consecutive sinusoid peaks by comparing the variation length scales: to order of magnitude, we can expect α_0 to vary by of order α_0 on scales of $1/\Delta\kappa$, so that over one period of the sinusoid, $1/\overline{\kappa}$, it will vary by $\Delta\alpha_0 = \alpha_0 \Delta\kappa/\overline{\kappa} = \alpha_0/R$, where R is the spectrograph resolution. Since for any input spectrum, $1/\Delta\kappa$ determines the fastest variation scale for the envelope, this represents an upper limit. For the ET instruments, $R \sim 5000$, so that over the length of the slit (a few fringes) $\Delta\alpha_0/\alpha_0 \sim 10^{-3}$. In practice, such a small variation will usually be significantly below the measurement errors in fringe phase and visibility due to photon noise for even the brightest sources, and would correspond to a final velocity error of $\sim$0.1 m s^{-1} for an instrument similar to the KPNO ET.[10] Even in the event that it is desired to reach such extremely high signal-to-noise ratios (S/Ns), it is in principle a simple matter to fit extra parameters to allow for non-uniformity of the sinusoidal fringe, although this has not been attempted with the ET instruments.

In Figure 2, the varying amplitude of the modulating coherence envelope, $\boldsymbol{\alpha}_0$, is illustrated explicitly, and we see how measuring the fringe over a narrow range of delays Δd around d_0 gives an approximately uniform sinusoid. This corresponds directly to the image seen along the length of the slit direction in a given channel on the detector. For illustration the very simple case is shown of white light with through a rectangular bandpass with no absorption lines, so that Q (and therefore Q_0) is a top-hat function. $\boldsymbol{\alpha}_0(d)$, therefore, is the corresponding Fourier transform, a sinc function, with zeros at $d = n/\Delta\kappa (n \in \mathbb{Z}^+)$, which modulates a sinusoid of period $1/\overline{\kappa}$. In practice the passband, $\Delta\kappa/\overline{\kappa}$, will be very narrow, so that the variation of $\boldsymbol{\alpha}_0$ will be much slower compared with the sinusoid than suggested in the figure, and the sinusoid itself will be highly uniform over Δd (i.e., over the length of the slit).

For a more complicated input spectrum, such as that from a star with its multitude of absorption lines, and for a more realistic LSF, the coherence envelope will generally also have a much more complicated shape, though the variations will still be slow in d and therefore close to uniform along the slit (i.e., within the upper limit discussed above, since the width of the resolution element still determines the fastest variation scale). Each channel will have its own unique piece of spectrum contributing to it, and therefore each will have its own particular phase and visibility. It is this that gives rise to the varied patterns of fringes that are seen in the final fringing stellar spectra (e.g., Figure 1(F)).

In practice, the profile in the slit direction will also be modulated in amplitude by a slit illumination function, but this can be calibrated out or modeled during the fringe fitting, and has no effect on fringe visibility. Though this can present its own practical challenges for data reduction, the illumination function is neglected here for simplicity, and taken to be uniform and equal to unity.

As an aside we note that $\boldsymbol{\alpha}_0$ and $\boldsymbol{\alpha}$ are very closely related: from their respective definitions in Equations (6) and (3), $\boldsymbol{\alpha}_0(d) = e^{i2\pi d\overline{\kappa}}\boldsymbol{\alpha}(d)$. The only difference is a phase offset, which, for a given channel j at wavenumber $\overline{\kappa}_j$ and fixed delay $d = d_0$, is constant—that is to say, $\alpha_0 = \alpha$ and $\phi_{\alpha_0} = \phi_\alpha + 2\pi d_0 \overline{\kappa}_j$. Since the instrument is to be used purely for differential measurements, the zero point from which phases are measured is somewhat arbitrary and has no physical significance: we are concerned with *changes* in phase over time, which will affect both $\boldsymbol{\alpha}_0$ and $\boldsymbol{\alpha}$ in the same way. For the analyses presented hereafter, the difference between $\boldsymbol{\alpha}_0$ and $\boldsymbol{\alpha}$ is therefore not of great significance, and either can equally well be thought of as the complex visibility. However, for the sake of consistency, $\boldsymbol{\alpha}$ is generally intended by the term.

2.3. From Phase to Velocity

To recap, in general, for a given channel j on the detector, the complex visibility of the measured fringe is given as in

[10] Assuming $\sim$1000 independent channels, phase–velocity scaling factor $\Gamma \approx 3300$ m s^{-1} rad^{-1} (see Section 2.3), and using the relationship between phase error and visibility error shown in Section 3.1, Equation (36), so that the expected error is $\Gamma\varepsilon_{\phi,j}/\sqrt{1000} = 10^{-3}\Gamma/\sqrt{1000}$.

Equation (3) (or see Goodman 1985, chap. 5). We can rewrite this as

$$\boldsymbol{\alpha} = \frac{\mathcal{F}[P_\kappa w_{\kappa j}]_{d=d_0}}{\mathcal{F}[P_\kappa w_{\kappa j}]_{d=0}} = \frac{\mathcal{F}[P_\nu w_{\nu j}]_{\tau=\tau_0}}{\mathcal{F}[P_\nu w_{\nu j}]_{\tau=0}}, \quad (8)$$

where $\boldsymbol{\alpha}$ is the complex visibility (or complex degree of coherence), a vector quantity whose phase represents the phase of the measured fringe, and whose magnitude (from 0 to 1) represents the absolute visibility of the measured fringe; $\mathcal{F}[\ldots]_\ldots$ represents a Fourier transform evaluated at interferometer path difference d, or time delay τ, where $d = c\tau$ and c is the speed of light; P is the input spectrum; and w_j is the response function for that particular channel on the detector, so that the spectrum contributing to the channel is given by $Q_j = Pw_j$ as before. We take d to be fixed at a value d_0 (for the purposes of the calculations here, the small difference in d across the length of a sinusoidal fringe is of no consequence). Subscripts are added to explicitly indicate functions of wavenumber, κ, or optical frequency, $\nu = c\kappa$: we note that the equation is completely equivalent in κ space with d as the conjugate variable, or in ν space with τ as the conjugate variable. In general, the form being used will be implicit from the context, so we drop these subscripts. We have also replaced the integral over the flux in the denominator with the Fourier transform at zero delay, which is mathematically equivalent (this fact is made use of a number of times later on in this analysis). All the necessary mathematics for determining Doppler shifts and for dealing with the combination of the star and fiducial reference spectra (see Section 2.6) derive from this formula.

The key to the DFDI RV technique is the fact that Doppler shifts of the spectrum result in directly proportionate phase shifts of the fringes. This is a direct consequence of the Fourier shift theorem (see, e.g., Erskine 2003). If the spectrum shifts such that $P(\kappa) \rightarrow P'(\kappa) \equiv P(\kappa + \Delta\kappa)$, and we correctly follow the shift in the dispersion direction (so that we now compare to the wavelength channel corresponding to $w_{j+\Delta j} = w_j(\kappa + \Delta\kappa)$—assuming that the spectrograph response function maintains the same form in nearby channels, and noting that Δj is not necessarily an integer), then the shift theorem gives

$$\begin{aligned}\boldsymbol{\alpha}' &= \frac{\mathcal{F}[P(\kappa+\Delta\kappa)w_j(\kappa+\Delta\kappa)]_{d=d_0}}{\mathcal{F}[P(\kappa+\Delta\kappa)w_j(\kappa+\Delta\kappa)]_{d=0}} \\ &= e^{i2\pi\Delta\kappa d_0}\frac{\mathcal{F}[P(\kappa)w_j(\kappa)]_{d=d_0}}{\mathcal{F}[P(\kappa)w_j(\kappa)]_{d=0}} = e^{i2\pi\Delta\kappa d_0}\boldsymbol{\alpha}. \quad (9)\end{aligned}$$

In other words, we have a phase shift of $\Delta\phi = 2\pi d_0\Delta\kappa$. By comparing the measured phase of the new fringes $\boldsymbol{\alpha}'$ with the previously unshifted ones, $\boldsymbol{\alpha}$, it is thus possible, in this simple case where there is no superposed reference spectrum and the instrument is perfectly stable, to derive the Doppler shift without any explicit knowledge of the underlying high-resolution spectrum, or of the spectrograph LSF. Using the Doppler shift equation $\Delta\kappa/\kappa \approx -\Delta v/c$, where v represents velocity, conventionally positive in the direction away from the observer, we can write

$$\Delta\phi = 2\pi d_0\Delta\kappa = -\frac{2\pi d_0\kappa\Delta v}{c} = -\frac{2\pi d_0}{c\lambda}\Delta v \equiv \frac{\Delta v}{\Gamma}, \quad (10)$$

where, Γ, the phase–velocity scaling factor which gives the proportionality between phase shift and velocity shift, is defined as

$$\Gamma \equiv -\frac{c\lambda}{2\pi d_0}. \quad (11)$$

By combining the many measurements of the phase shift $\Delta\phi$ from each channel, j, (allowing, if necessary, for the wavelength dependence of Γ), a very high precision measurement of the differential Doppler velocity shift, Δv, can be made.

2.4. The Interferometer Comb

The interferometer comb, mentioned in Figure 1 and the corresponding text, is really just a special case of the discussion in Section 2.2, where the input spectrum to the instrument is purely white light continuum. In that case Q, the product of the input spectrum and the spectrograph response function, is itself equal to the spectrograph response function. The comb is therefore purely a consequence of the response function, arising naturally from Equation (3). In fact, the example used of the top-hat function for Q is a reasonable first approximation for the LSF, and so also for the response function (see Appendix A), for a spectrograph where the slit width dominates the resolution. The interferogram in Figure 2 is thus a reasonable representation of the behavior of the interferometer comb at finite resolution.

We can see from this that by appropriately choosing the delay and spectrograph slit width we can null out the interferometer comb by finding a minimum in the envelope. Early experiments changing the slit width and delay with ET prototypes did indeed show this kind of sinc-like variation in the comb visibility. This becomes important when using a superimposed reference spectrum, as in Section 2.6.1.

It is also instructive to consider an idealized infinite resolution spectrograph. In this case, the response function, w_j, becomes a delta function, so that Q_j is also a delta function for all channels j. By Equation (6), given that Q_0 is the delta function shifted to $d = 0$, the coherence envelope, $\boldsymbol{\alpha}_0(d)$, is the normalized Fourier transform of this delta function: $\boldsymbol{\alpha}_0(d) = 1$ at all delays. Equation (7) then gives the very simple form of the resulting interferogram:

$$I_{\rm norm} = 1 + \cos(2\pi d\kappa), \quad (12)$$

where we have stopped representing $\overline{\kappa}$ as a mean value since the width of the channel is negligible.

This 100% visibility "infinite resolution" comb is the underlying form for any DFDI comb. Lowering the resolution will reduce the visibility from 100% at the given fixed delay, as in the example of Figure 2, with perhaps an overall phase offset depending on the symmetry of the spectrograph response function (and uniform to the extent that the response function and LSF are uniform across all channels).

The infinite-resolution comb can also be thought of as a an interferometer transmission function. In introducing the instrument (Section 2.1), we first described the formation of the DFDI spectrum as a multiplication of the stellar spectrum and the infinite-resolution interferometer comb (i.e., interferometer transmission function), convolved with the LSF down to the spectrograph resolution. This is the approach adopted by Erskine (2003) and Mahadevan (2006), and both views are entirely equivalent. Following the Fourier transform approach outlined here, however, we can proceed somewhat further, and obtain some important insights in understanding systematic errors from the use of a simultaneous fiducial reference spectrum (Section 2.6). In principle, the Fourier transform approach can also be used to create simulated DFDI spectra without having to assume a uniform LSF at all wavelengths, which is difficult

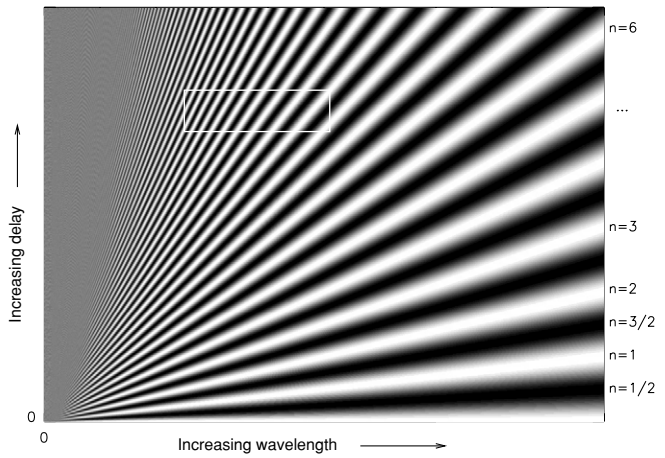

Figure 3. Simulated interferometer comb, as a function of wavelength (corresponding with dispersion direction on detector) and delay (corresponding with slit direction). Setting a large interferometer delay and choosing the wavelength range over which the spectrum is observed selects a "window" in the comb (shown schematically) where the fringes are approximately parallel. The orders of some of the fringes, n, are shown down the right-hand side. In practice, the "window" chosen is at much longer wavelength and much higher order.

to do in the alternative approach. A derivation relating the two methods is outlined in Appendix B.

To show visually how the comb forms, it is depicted schematically in Figure 3, plotting contours of flux from Equation (12) as a function of wavelength $\lambda = 1/\kappa$ and delay d. Since λ maps linearly to x-position on the detector and delay maps linearly to y-position along the slit (at least for an ideal spectrograph and interferometer), this also represents the image that would be seen on the detector if the full ranges could be sampled down to zero wavelength and zero delay. The box in the figure schematically represents the segment of the interferogram that we actually observe with the instrument: a series of tilted parallel fringes (as shown in Figure 1(D)), with a very slow wavelength dependency. For clarity, the figure is not to scale: in practice, the delay is fixed to a much larger value so that the fringes are observed at much higher order, n, and the wavelengths observed are much longer, so that any real observed comb is much denser and more uniform, and the variations with wavelength much smaller.

2.5. Calculating the Interferometer Delay

The interferometer delay, d_0, is determined by the etalon in the interferometer, and must be precisely known in order to be able to accurately translate from phase measurements to velocity measurements. The best precision that can be obtained in RV measurements is a trade-off between maximizing the phase–velocity scale Γ (so that a large phase shift results from a small change in velocity) and maximizing the visibility of the fringes (since higher visibility means more accurate measurements of the fringe phases). Since the visibility of the fringes is determined by the match between d_0 and the typical spectral line widths to be observed, an optimal value of d_0 can be chosen to give the best precision for the expected typical targets for the survey (Ge 2002). This is set at design time, and remains fixed for the instrument.

Annual variations in the RV of a star can be as large as $\sim$60 km s^{-1} even for an RV-stable target, owing simply to the orbital motion of Earth around the Sun (which dominates significantly over Earth's rotation). If we are to consider approaching precisions on the order of 1 m s^{-1} we therefore need to know Γ to better than one part in 60,000. Since Γ depends directly on the interferometer delay (Equation (11)), determining Γ is synonymous with measuring the delay.

To a first approximation, the delay can be calculated from the properties of the delay in the interferometer. For example, for a monolithic interferometer with arm lengths L_1 and L_2 and refractive indices n_1 and n_2 respectively, this is given by Mahadevan et al. (2008a):

$$d_0 = 2(n_1 L_1 - n_2 L_2). \tag{13}$$

This depends on the assumption that there is negligible dispersion in the etalon glass, i.e., that n_1 and n_2 are close to independent of wavelength over the wavelength range of interest. Dispersion can in fact be a significant effect, but the assumption should be good to a few percent (Barker & Schuler 1974; D. J. Erskine 2001, private communication), enough for an initial estimate. Fully accounting for the dispersion and allowing d_0 to become a function of wavelength, however, is essential where very high velocity precision is required from large bandwidth observations.

A more precise measure of the delay can be determined simply by counting fringes in the interferometer comb. We know from Equation (12) that the phase of the comb varies as $\phi = 2\pi d\kappa = 2\pi d/\lambda$. Although this equation is for a comb at infinite resolution, the same variation will hold true at lower resolutions: a spectrograph response function broader than a delta function will only reduce the visibility of the interferogram, and possibly add an overall phase offset to the entire interferogram (provided that the shape of the response function is uniform across the detector). Differentiating with respect to wavelength:

$$\frac{\partial\phi}{\partial\lambda} = \frac{\partial(2\pi n)}{\partial\lambda} = -\frac{2\pi d}{\lambda^2}, \tag{14}$$

where $n = \phi/2\pi$ is the fringe order, giving

$$d = -\lambda^2 \frac{\partial n}{\partial\lambda}. \tag{15}$$

In other words, by counting the fringe density $\partial n/\partial\lambda$ over wavelength, we can immediately calculate d_0, and hence Γ. Since there is a λ^{-2} dependence in $\partial n/\partial\lambda$ itself, care needs to be taken to account for the dependence properly when determining the fringe density at a given wavelength. This may more easily be done in wavenumber space instead, since the fringe density is uniform with wavenumber, and $d = \partial n/\partial\kappa$.

In practice, counting fringes is often not easy, since the comb is often barely resolved (usually by design). As long as the comb is not undersampled on the detector, this can be overcome by temporarily using a narrower slit in the spectrograph, since in principle the delay should only need to be determined once. Even so, it is usually possible in practice only to count over a range of a few hundreds to one or two thousand fringes. Counting along one row in the dispersion direction of the comb therefore gives an accuracy on the order of one part in 1000. Over a 60 km s^{-1} variation, this is still only good to the 60 m s^{-1} level. Our method of choice in the past has been simply to observe known stable reference stars over the time baseline of interest and use their known apparent changes in velocity due to Earth's motion to calibrate Γ. Provided the reference stars are genuinely stable, and they are positioned in the sky such that their barycentric motions are large, this technique will provide an accuracy in the determination of Γ at least equal to the intrinsic RV stability of the stars.

Other methods are under investigation which should allow more precise measurement of the delay. By averaging fringe counts over many rows of a wide spectrum, and further averaging over many frames, it may be possible to achieve significantly sub-fringe counting accuracy (J. Wang et al. 2010, in preparation). Other techniques in development using a separate device to directly measure the interferometer delay should provide a robust direct measurement that obviates the need for more laborious empirical delay determination (X. Wan et al. 2010, in preparation).

2.6. Handling a Fiducial Reference Spectrum

2.6.1. Multiplied Reference

The extremely high sensitivity of the instrument means that numerous instrumental effects can masquerade as velocity shifts. Tiny changes in the interferometer delay due to thermal flexure, for example, will appear as phase shifts in the fringe pattern. The image itself can also shift as a whole on the detector in both the slit and the dispersion directions.

One way of accounting for these instrumental artifacts is to use a fiducial spectrum from some known zero-velocity reference. The simplest way to do this is to bracket the science data, either spatially, running the fiducial spectra along a separate optical path alongside the target spectrum; or temporally, alternating target exposures and reference spectrum exposures along the same optical path. Since the reference spectrum is stationary with respect to the instrument, it will track instrument shifts, which can then be subtracted from the measured stellar shift to reveal the star's intrinsic motion. (Note that from Equation (10), a change in d_0 conveniently has mathematically exactly the same effect as a change in velocity, Δv.) These approaches, however, potentially suffer from errors due to their separation from the science data: in the first case, because of non-common path errors due to imperfect optics, and in the second case, because the fiducial exposures are not tracking instrument drift contemporaneously with the data.

An alternative approach is to insert an absorption reference into the optical path—in the case of the ET instruments in the past, a glass cell filled with iodine vapor maintained at a fixed temperature, the traditional reference of choice for RV planet searches. In this way, the reference spectrum is multiplied with the stellar spectrum. To do this, for each target to be observed, two fringing "template" spectra are taken, one being pure star with no reference in the beam path, and the other pure reference (for ET, a pure iodine spectrum taken by shining a tungsten continuum lamp through the cell). These templates are then used to separate out the stellar and reference components of the combined star/reference data (referred to here as "data" or "measurement" frames, as distinct from "template" frames). A formalism is required to extract the reference and stellar spectra from the combined spectrum. In order to proceed, we define the following symbols.

1. j—as before, the pixel number in the dispersion direction which identifies the column along which a fringe is measured in the slit direction, corresponding to a single channel. Strictly speaking, the channel is infinitesimally wide on the detector, so that j need not necessarily be an integer. Since the spectrum is oversampled, however, it is often a reasonable simplification to think of the entire pixel column representing an infinitesimal sample in the dispersion direction (see Appendix A).
2. $\mathbf{M}(j)$—the complex visibility vector (i.e., phase and absolute visibility) for a fringe at channel j in a single Doppler measurement frame of combined star/reference data, an ensemble of such values for a spectrum across all j comprising a "whirl."
3. $\mathbf{S}(j)$—the measured complex visibility for the star template at channel j.
4. $\mathbf{I}(j)$—the measured complex visibility for the reference template at channel j.
5. $\mathcal{M}(\lambda) \equiv C_{\rm m}(\lambda)M(\lambda)$—the input spectrum for a combined star/reference data frame, where $C_{\rm m}$ represents a normalization, such as the continuum function, and M is the normalized spectral density. $C_{\rm m}$ is assumed constant to a good approximation over the scale of the width of the response function w (see below) and instrument LSF, and $0 \leqslant M \lesssim 1$.
6. $\mathcal{S}(\lambda) \equiv C_{\rm s}(\lambda)S(\lambda)$—the same for the star template spectrum.
7. $\mathcal{I}(\lambda) \equiv C_{\rm i}(\lambda)I(\lambda)$—the same for the reference template spectrum.
8. $s(\lambda)$, $i(\lambda)$—such that $S \equiv 1-s$, $I \equiv 1-i$; $0 \leqslant (s, i) \leqslant 1$.
9. $w(j, \lambda)$—the response function at position j on the detector, i.e., the spectrum that contributes to an infinitesimally wide channel at the detector plane if perfect continuum light is passed through the instrument. (Note that w is very closely related to the instrument LSF—see Appendix A).
10. d—the interferometer delay, fixed to a value of $d = d_0$, as usual.
11. Γ—phase/velocity scaling constant, also as before.
12. $\mathcal{F}[\ldots]_d$—as before, Fourier transform evaluated at interferometer path difference d.
13. $\widehat{\ldots}|_d$—shorter notation for Fourier transform, for convenience.
14. $[\ldots \otimes \ldots]|_d$—used to denote convolution, evaluated at a delay of d.

We assume for now the case where there is neither intrinsic Doppler shift nor any instrument shift in either phase or in the dispersion direction, for both star and reference components. We also assume no photon shot noise. Here the aim is simply to reconstruct the data whirl from the two template whirls. Once this is achieved, it is conceptually a relatively trivial step to allow for shifted and noisy data: the template whirls need only to be shifted iteratively in phase and translated in the dispersion direction until a best-fit solution is found, allowing the intrinsic stellar Doppler shift to be directly calculated. This can be done using any standard least-squares method.

Following Equation (8), the complex visibility measured at detector channel j for the two templates, $\mathbf{S}$ and $\mathbf{I}$, and the combined star/reference data, $\mathbf{M}$, can be written exactly as

$$\mathbf{S} = \frac{\mathcal{F}[\mathcal{S}w]_{d_0}}{\mathcal{F}[\mathcal{S}w]_0} = \frac{[\widehat{\mathcal{S}} \otimes \widehat{w}]|_{d_0}}{[\widehat{\mathcal{S}} \otimes \widehat{w}]|_0}, \tag{16}$$

$$\mathbf{I} = \frac{\mathcal{F}[\mathcal{I}w]_{d_0}}{\mathcal{F}[\mathcal{I}w]_0} = \frac{[\widehat{\mathcal{I}} \otimes \widehat{w}]|_{d_0}}{[\widehat{\mathcal{I}} \otimes \widehat{w}]|_0}, \tag{17}$$

$$\mathbf{M} = \frac{\mathcal{F}[\mathcal{M}w]_{d_0}}{\mathcal{F}[\mathcal{M}w]_0} = \frac{\mathcal{F}[\mathcal{S}\mathcal{I}w]_{d_0}}{\mathcal{F}[\mathcal{S}\mathcal{I}w]_0} = \frac{[\widehat{\mathcal{S}} \otimes \widehat{\mathcal{I}} \otimes \widehat{w}]|_{d_o}}{[\widehat{\mathcal{S}} \otimes \widehat{\mathcal{I}} \otimes \widehat{w}]|_0}. \tag{18}$$

The key lies in expressing Equation (18) in terms of Equations (16) and (17). This is made difficult by the convolutions, which appear to require knowledge of the template

spectra at all possible values of the delay d in order to be evaluated. The nature of the DFDI is such that we measure it only at one value, d_0. An approximation can be used to address this problem, which is described in Section 2.6.1.

It is possible to rewrite the input spectrum as

$$\begin{aligned}\mathcal{M} &= A\mathcal{S}\mathcal{I} \\ &= AC_{\rm s}C_{\rm i}SI \equiv C'SI \\ &= C'(1-s)(1-i) \\ &= C'(1-s+1-i-1+si) \\ &= C'(S+I-1+si),\end{aligned} \tag{19}$$

where A is a scaling constant to allow for difference in total flux level between the templates and data, and $C' \equiv AC_{\rm s}C_{\rm i}$ is a constant over the width of the response function. If we assume either s or i or both $\ll 1$, then the "cross-talk" term, si, can be neglected. Since i and s essentially represent line depths, this means that we are assuming either very shallow lines, or no significant overlap between lines in the two different spectra. Keeping the cross-talk term in place for now for completeness, however, we can continue, substituting Equation (19) in the first expression on the right-hand side of Equation (18):

$$\mathbf{M} = \frac{\mathcal{F}[\mathcal{M}w]_{d_0}}{\mathcal{F}[\mathcal{M}w]_0} = \frac{[\widehat{Sw} + \widehat{Iw} - \widehat{w} + \widehat{siw}]|_{d_0}}{[\widehat{Sw} + \widehat{Iw} - \widehat{w} + \widehat{siw}]|_0}. \tag{20}$$

The factor C' has canceled because it is constant over the width of the response function, and therefore can be taken outside the Fourier transforms. The denominator of this equation represents a normalization, corresponding to the total flux in channel j on the detector. The term $\widehat{w}|_{d_0}$ in the numerator is due to the interferometer comb, since if white light is passed through the instrument, then $S = I = 1$, and the cross-talk term vanishes. We are then left with

$$\mathbf{M}_{\rm continuum} = \widehat{w}|_{d_0}/\widehat{w}|_0, \tag{21}$$

which describes the interferometer comb. As expected, the properties of the comb are determined purely by the response function, as discussed in Section 2.4. There the comb was described first for a delta-function response function, and then for a top hat; the equation here represents the generalization to any shape of response function.

Rewriting the first expression on the right-hand side of Equations (16) and (17) in terms of S and I and substituting into Equation (20), we can write

$$\mathbf{M} = K_{\rm s}\mathbf{S} + K_{\rm i}\mathbf{I} \quad + \quad \frac{-\widehat{w}|_{d_0} + \widehat{siw}|_{d_0}}{\widehat{Sw}|_0 + \widehat{Iw}|_0 - \widehat{w}|_0 + \widehat{siw}|_0}, \tag{22}$$

where the scalar quantities $K_{\rm s}$ and $K_{\rm i}$ are given by

$$\begin{aligned}K_{\rm s} &\equiv \frac{\widehat{Sw}|_0}{\widehat{Sw}|_0 + \widehat{Iw}|_0 - \widehat{w}|_0 + \widehat{siw}|_0}, \\ K_{\rm i} &\equiv \frac{\widehat{Iw}|_0}{\widehat{Sw}|_0 + \widehat{Iw}|_0 - \widehat{w}|_0 + \widehat{siw}|_0}.\end{aligned} \tag{23}$$

Hence we see that we can now represent the combined star/reference data in terms of a linear combination of the measured star and reference templates, along with an error term.

The fraction on the right in Equation (22) contains two terms in the numerator, the comb term, $\widehat{w}|_{d_0}$, and a cross-talk term, $\widehat{siw}|_{d_0}$. It is in principle possible to arrange the instrument such that at delay $d = d_0$ the interferometer comb has zero visibility, by choosing the delay and slit width so that $\mathbf{M}_{\rm continuum}$ is at a zero point of $\widehat{w}$ (see Section 2.4). Alternatively, it is possible to low-pass Fourier filter the data image before measuring the whirls, essentially simulating a lower spectrograph resolution. In either case, we assume that $\widehat{w}|_{d_0} \to 0$. If we now also neglect all the cross-talk terms si following from Equation (19), we finally have the whirl addition approximation, which we can write as

$$\mathbf{M} \approx K_{\rm s}\mathbf{S} + K_{\rm i}\mathbf{I}. \tag{24}$$

$K_{\rm s}$ and $K_{\rm i}$ represent scaling factors in the absolute visibilities of the two templates. In the case that we take our normalization functions ($C_{\rm m}$, $C_{\rm s}$, and $C_{\rm i}$) to be continuum normalization functions, then remembering that the evaluation of a Fourier transform at $d = 0$ represents the total integrated area under the function, we can try to gain a handle on the expected sizes of these scaling factors. To the extent that the total area under Sw and Iw is not much less than that under w (i.e., that the area in discrete absorption lines is small, or $\int_{\Delta w} s d\lambda \ll 1$ and $\int_{\Delta w} i d\lambda \ll 1$, where Δw is a representative width of the response function), Equation (23) implies that $K_{\rm s}$, $K_{\rm i} \approx 1$. This can easily be seen by rewriting in terms of s and i alone: we can then assume all the terms $\widehat{sw}|_0$, $\widehat{iw}|_0$, $\widehat{siw}|_0 \ll 1$—the last because both s and i are everywhere less than 1 by definition and so si must always be even smaller than either—and we find we are then left with $K_{\rm s} \approx \widehat{w}|_0/\widehat{w}|_0 = 1$, and likewise for $K_{\rm i}$.

As far as the addition approximation holds good, and to the extent that $K_{\rm s}$ and $K_{\rm i}$ are approximately constant across all channels j, it is then a simple matter to allow for Doppler and instrument drift by allowing the template whirls to rotate in phase and translate in the dispersion direction as a function of j; allowing $K_{\rm s}$ and $K_{\rm i}$ to vary as free parameters as well, we can minimize χ^2 in the residuals to find the best-fit solution compared to the measured data $\mathbf{M}$ for the complete ensemble of wavelength channels. The difference between the phase rotation of the star and that of the iodine (remembering to account for wavelength dependence as necessary) yields the intrinsic differential stellar Doppler shift, while the shifts in the dispersion direction allow for Doppler shift of the stellar lines and any instrumental image drift on the detector.

By these definitions, however, there is in fact little reason to assume that $K_{\rm s}$ and $K_{\rm i}$ should be constant from channel to channel. Furthermore, an iodine cell reference typically absorbs a total of ~40% of the incident light, so that the assumption of small area within the absorption lines is not necessarily robust across the whole spectrum. Inspecting the terms in a little more detail, we can recast them, rewriting Equation (23) as

$$K_{\rm s} = \frac{\widehat{Sw}|_0}{\widehat{\mathcal{M}w}|_0} = \frac{\mathcal{F}[(\mathcal{S}/C_{\rm s})w]_0}{\mathcal{F}[(\mathcal{M}/C_{\rm m})w]_0} = \frac{C_{\rm m}}{C_{\rm s}}\frac{\widehat{Sw}|_0}{\widehat{\mathcal{M}w}|_0}, \tag{25}$$

and likewise for K_i so that we have

$$K_{\rm s} = \frac{C_{\rm m}}{C_{\rm s}}\frac{\widehat{Sw}|_0}{\widehat{\mathcal{M}w}|_0}, \qquad K_{\rm i} = \frac{C_{\rm m}}{C_{\rm i}}\frac{\widehat{\mathcal{I}w}|_0}{\widehat{\mathcal{M}w}|_0}. \tag{26}$$

The terms are now written in terms of measurable quantities, namely the total fluxes in each channel j for the templates and the data. We also see that they are dependent on the definition of the functions $C_{\rm m}$, $C_{\rm s}$, and $C_{\rm i}$. Continuum normalization functions could be determined by simply fitting a smooth continuum function to the measured fluxes. There is, however, nothing

in the preceding analysis that *requires* that C_m, C_s, and C_i be continuum functions. Defining them as such allows for an intuitive approach to visualize the effect of absorption lines, but they can in fact be any function, subject only to our requirement that the fractional deviations of the spectra from these functions (as represented by s and i) remain small, so that the cross-talk term also remains small. It is arguably more appropriate to define the functions to represent the *mean flux* across each of their respective wavelength channels: in this case we see that K_s and K_i simplify immediately to exactly unity, independent of wavelength channel, so that they drop out of Equations (22) and (24). The difference is absorbed in the cross-talk term through its dependence on s and i, which in turn are also dependent on C_s and C_i, respectively. Written in this way, the whole of the addition approximation error is included in the single cross-talk term, $\widehat{si}\,\widehat{w}|_{d_0}$, in Equation (22).

We now have an approximate formalism for solving for stellar Doppler shifts from combined star/reference data, where the reference spectrum multiplies the stellar spectrum. The above analysis is only useful, however, in as far as the approximation that the cross talk, si, is very small holds well. It appears, however, that as it stands, this approximation is in fact not accurate enough for exoplanet searches. In Section 3.3.3, we derive an estimate of the errors resulting from the approximation, and find that systematics as large as 50 m s^{-1} or more can arise. Clearly this cannot be neglected. Approaches to correcting or avoiding the error are discussed in Section 4.

2.6.2. An Alternative: Combined-beam Reference

One possible solution to the problem of the addition approximation is to actually physically superpose a reference spectrum on top of the stellar target spectrum, for example, by splicing two input fibers into one, one coming from the telescope and one from the reference lamp. In this case, the two spectra now combine additively instead of multiplicatively. We can then write

$$\mathcal{M} = A_s\mathcal{S} + A_i\mathcal{I}, \tag{27}$$

where A_s and A_i are scaling factors to allow for flux differences between the templates and data (note that two such factors are now required). Once again, following Equation (8) we can now write

$$\begin{aligned}\mathbf{M} &= \frac{\mathcal{F}[\mathcal{M}w]_{d_0}}{\mathcal{F}[\mathcal{M}w]_0} \\ &= \frac{\mathcal{F}[(A_s\mathcal{S} + A_i\mathcal{I})w]_{d_0}}{\mathcal{F}[(A_s\mathcal{S} + A_i\mathcal{I})w]_0} \\ &= \frac{A_s\widehat{\mathcal{S}w}|_{d_0} + A_i\widehat{\mathcal{I}w}|_{d_0}}{A_s\widehat{\mathcal{S}w}|_0 + A_i\widehat{\mathcal{I}w}|_0},\end{aligned} \tag{28}$$

or alternatively,

$$\mathbf{M} = K_s'\mathbf{S} + K_i'\mathbf{I}, \tag{29}$$

where we define

$$K_s' \equiv \frac{A_s\widehat{\mathcal{S}w}|_0}{A_s\widehat{\mathcal{S}w}|_0 + A_i\widehat{\mathcal{I}w}|_0}, \qquad K_i' \equiv \frac{A_i\widehat{\mathcal{I}w}|_0}{A_s\widehat{\mathcal{S}w}|_0 + A_i\widehat{\mathcal{I}w}|_0}, \tag{30}$$

or

$$K_s' = A_s\frac{\widehat{\mathcal{S}w}|_0}{\widehat{\mathcal{M}w}|_0}, \qquad K_i' = A_i\frac{\widehat{\mathcal{I}w}|_0}{\widehat{\mathcal{M}w}|_0}. \tag{31}$$

We see that we now have an exact expression for **M**, with the difference being that we now need to take into account the flux scaling factors A_s and A_i, where previously the flux scaling factor had canceled.

There is also a constraint on the visibility scaling constants K_i' and K_s'. Since the Fourier transforms at $d = 0$ represent total fluxes within the channel, flux conservation means that we can write

$$A_s\widehat{\mathcal{S}w}|_0 + A_i\widehat{\mathcal{I}w}|_0 = \widehat{\mathcal{M}w}|_0. \tag{32}$$

Dividing through by the flux in the combined star/iodine data, $\widehat{\mathcal{M}w}|_0$, and substituting the visibility scaling constants, we find

$$K_i' + K_s' = 1. \tag{33}$$

As before, we can solve for phase rotation and dispersion shift by χ^2 minimization, this time additionally solving for the two flux scaling constants. It is interesting to note that if we multiply through both sides of Equation (29) by the denominator, $\widehat{\mathcal{M}w}|_0$ (which represents the total flux along the channel in the combined data), we essentially find we have an expression which is a summation of flux × visibility terms. Since visibility is defined as $(I_{max} - I_{min})/(I_{max} + I_{min})$, where I_{max} and I_{min} are the maximum and minimum fringe intensities, then multiplying by total flux in the channel gives a quantity equal to the amplitude of the fringe. Hence Equation (29) is really simply summing fringe amplitudes, and is exactly what we expect when the two input spectra are combined additively: the resulting image on the detector should simply be a direct flux summation of the respective images that would be obtained individually.

3. SOURCES OF ERROR

Here we provide derivations of some useful formulae for estimating the errors from certain sources for which we have been able to find analytical approaches. These include photon errors; additive spectral contamination errors, such as moonlight background, crowded targets, etc.; and multiplicative fringe-visibility contamination errors, which include in particular the cross-talk error due to the whirl addition approximation for in-beam absorption reference sources, but which can also be applied to other effects such as residual interferometer comb (again, in the case of an in-beam reference). The latter formulae are potentially applicable to a number of different error sources, and all are likely to be useful for any implementation of a DFDI instrument.

Since this is primarily a theory paper, we do not attempt to provide a comprehensive accounting of error sources: many are instrument implementation specific, or data reduction pipeline specific, and better suited to empirical or semi-empirical assessment through simulations and experimentation. Such work is still ongoing with the ET project. For more complete discussion of specific errors in the ET project, we point the reader to upcoming MARVELS publications on the instrument (J. Ge et al. 2010, in preparation) and pipeline (B. Lee et al. 2010, in preparation); more detailed discussions of errors from earlier ET work can also be found in van Eyken (2007) and Mahadevan (2006). Table 1 provides a summary of the examples of applications of the error formulae provided in the text.

3.1. Photon Errors

The errors due to photon shot noise provide an important baseline for any instrument. They indicate the absolute limit to the precision that can be achieved, and drive throughput and (for DFDI instruments) fringe visibility considerations

Table 1
Summary of Example Error Magnitudes

Noise Source	Subsection	Approx. Magnitude (m s^{-1})
Photon shot noise—multiplied ref.[a]	3.1.1	3.2
Photon shot noise—added ref.[a]	3.1.2	3.6
Photon shot noise—separate ref.[a]	3.1.3	2.9
Moonlight contamination	3.2.2	$\lesssim 41$
Residual interferometer comb[b]	3.3.2	9
Addition approximation[b]	3.3.3	50

Notes. Error magnitudes as calculated in the text are listed: these are examples for illustration only, and each is highly variable and dependent on specific circumstances. See the text for assumptions made in each case.
[a] Assuming iodine reference—see text for improvements using ThAr in the added-reference case.
[b] Applies only for multiplied reference spectrum.

for the optical design. It is entirely reasonable to conceive of a photon-limited DFDI-type instrument. However, even in cases where photon noise is dominated by other effects in the very high precision regime, photon noise inevitably becomes significant at the faint end of the stellar target sample. For the MARVELS/Keck ET, geared toward moderate precision surveys of fainter targets, although other errors dominate the instrument requirements error budget at the brightest ($V \sim 8$ mag) end of the target range, photon noise becomes a significant part of the error at fainter levels (down to $V = 12$ mag, $\sim$21.5 m s^{-1} of a total 35.0 m s^{-1}; see Ge et al. 2009). In the high precision, high-flux regime (e.g., a planned 1 m s^{-1}—level cross-dispersed DFDI upgrade for the KPNO ET), the photon error is also important as it indicates the level below which other sources of systematic and random error must be driven.

The photon error in the phase measurement (and hence velocity measurement) from a single channel can be estimated following Ge (2002). This gives essentially

$$\varepsilon_{v,j} \approx \frac{1}{\pi\sqrt{2}} \frac{c\lambda}{d\alpha_j\sqrt{F_j}} = \Gamma\frac{\sqrt{2}}{\alpha_j\sqrt{F_j}}, \tag{34}$$

where $\varepsilon_{v,j}$ is the error in velocity due to channel j alone, c is the speed of light, λ is the wavelength, d is the optical delay, α_j is the visibility of the fringe, F_j is the total flux in the channel, and Γ is the usual phase–velocity scaling factor (Equation (11), ignoring the negative sign since we are interested only in the magnitude).[11] The terms following the Γ represent the error in phase due to the photon noise, $\varepsilon_{\phi,j} = \sqrt{2}/(\alpha_j\sqrt{F_j})$. Following a similar derivation, it is straightforward to show that the error in *visibility* due to photon noise, $\varepsilon_{\alpha,j}$, is given by

$$\varepsilon_{\alpha,j} = \sqrt{\frac{2}{F_j}}, \tag{35}$$

and hence, assuming independent errors, there is a useful simple relationship between the errors in phase and visibility:

$$\varepsilon_{\phi,j} = \frac{\varepsilon_{\alpha,j}}{\alpha_j}. \tag{36}$$

[11] The small difference in the numerical factor in the denominator of Equation (34) ($\pi\sqrt{2}$ versus 4) is due to using the rms slope of the fringe, rather than the mean absolute slope used in Ge (2002). Monte Carlo simulations of sinusoid fits suggest that the rms slope gives more accurate results.

As a general rule, we can see from Equation (34) that precision goes with the inverse root of flux, as one would expect, and also as the inverse of visibility: higher flux and/or higher visibility mean better precision. From this formula we can derive the photon errors in the final differential RV for different calibration scenarios.

For simplicity in the following formulae, we take λ to be constant, taking the wavelength value at the center of the spectrum, since it varies by only $\sim$10% from one end of the spectrum to the other in the current ET instruments. For an instrument with a very large bandwidth, however, it may be necessary to consider it properly as a function of channel, λ_j. This simply means it cannot be taken outside the brackets as in the following derivations, but otherwise the formalism is the same.

3.1.1. Photon Error for Multiplied Reference

To calculate the expected error in an RV measurement for a single data frame, assuming an instrument configuration where an iodine or other reference spectrum multiplies the input stellar spectrum, we consider the resulting data spectrum as consisting of two components, a star component and an iodine component. The calculated phase shift due to intrinsic target Doppler shift, $\Delta\phi$ is given by

$$\Delta\phi = \langle\phi_{\mathrm{sm},j} - \phi_{\mathrm{st},j}\rangle - \langle\phi_{\mathrm{im},j} - \phi_{\mathrm{it},j}\rangle, \tag{37}$$

where $\langle\ldots\rangle$ here represents a *weighted* mean over all j, $\phi_{\mathrm{sm},j}$ and $\phi_{\mathrm{im},j}$ represent the phases for the star and iodine components of the combined star/iodine data ("measurement") frame, and $\phi_{\mathrm{st},j}$ and $\phi_{\mathrm{it},j}$ are the phases measured in the separate pure star and iodine templates. For convenience, we immediately map these phases to corresponding "velocity" measurements by multiplying both sides by Γ to give a velocity shift, Δv (though with the caveat that a velocity measurement of a single channel in a single spectrum has no physical meaning in itself until it is differenced with another spectrum):

$$\Delta v = \langle v_{\mathrm{sm},j} - v_{\mathrm{st},j}\rangle - \langle v_{\mathrm{im},j} - v_{\mathrm{it},j}\rangle. \tag{38}$$

Using ε_v with corresponding subscripts to represent the various errors in this equation, we can expect a total photon error in Δv to be given by

$$\varepsilon_v^2 = \left[E_j\left(\sqrt{\varepsilon_{v,\mathrm{sm},j}^2 + \varepsilon_{v,\mathrm{st},j}^2}\right)\right]^2 + \left[E_j\left(\sqrt{\varepsilon_{v,\mathrm{im},j}^2 + \varepsilon_{v,\mathrm{it},j}^2}\right)\right]^2, \tag{39}$$

where $E_j(\sigma)$ represents the standard statistical error in a weighted mean:

$$E_j(\sigma_j) \equiv \frac{1}{\sqrt{\sum_j 1/\sigma_j^2}}. \tag{40}$$

In practice, the two template terms in Equation (39) are neglected, for two reasons. The first is simply because in general the templates will have significantly higher flux than the data frame: the iodine template can be taken with arbitrarily high flux since it is obtained with a quartz lamp as a source; and the stellar template is usually deliberately taken with higher flux than the data so that it does not compromise the entire data set. The second reason is a little more subtle. All RV measurements with this kind of instrument are differential, measured relative to the two templates which effectively set the zero point of the

measurements for the star and iodine, as seen in Equation (38). Since this "zero point" is the same for every RV measurement, any error in the zero point will not contribute to the rms scatter in a set of measurements which uses the same templates.

This last statement holds true to a point: accuracy in the templates is still needed in order to disentangle the stellar and iodine components of the combined data. From simulations of ET fringing spectra, we find, for example, that for a multiplied iodine reference, using a G0 or G2V stellar template in place of a G8V template yields an rms error of 11 m s^{-1} over large (60 km s^{-1}) differential velocity shifts. (Depending on the precision required, this points toward the interesting possibility of using templates of different stars from the target star: this could allow, for example, for higher S/N templates when observing very faint targets, or perhaps for disentangling the signals from double-lined spectroscopic binaries.)

Since photon errors go as $1/\sqrt{\text{flux}}$, the remaining terms, $E_j(\varepsilon_{v,\mathrm{sm}})$ and $E_j(\varepsilon_{v,\mathrm{im}})$, can be estimated by scaling the respective template errors (which, unlike the measurement component errors, can be determined directly from Equation (34)) by the flux difference between the templates and data, giving

$$\varepsilon_v^2 = [E_j(\varepsilon_{v,\mathrm{sm},j})]^2 + [E_j(\varepsilon_{v,\mathrm{im},j})]^2 \tag{41}$$

$$\approx \frac{\overline{F}_{\mathrm{st}}}{\overline{F}_{\mathrm{m}}}\,[E_j(\varepsilon_{v,\mathrm{st},j})]^2 + \frac{\overline{F}_{\mathrm{it}}}{\overline{F}_{\mathrm{m}}}\,[E_j(\varepsilon_{v,\mathrm{it},j})]^2, \tag{42}$$

where $\overline{F}_{\mathrm{st}}$, $\overline{F}_{\mathrm{it}}$, and $\overline{F}_{\mathrm{m}}$ represent the mean fluxes across the whole star template, iodine template and data frame, respectively. Explicitly substituting Equation (34) into Equation (42), we find

$$\varepsilon_v = \Gamma\sqrt{2}\sqrt{\frac{\overline{F}_{\mathrm{st}}}{\overline{F}_{\mathrm{m}}}\left[E_j\left(\frac{1}{\alpha_{\mathrm{st},j}\sqrt{F_{\mathrm{st},j}}}\right)\right]^2 + \frac{\overline{F}_{\mathrm{it}}}{\overline{F}_{\mathrm{m}}}\left[E_j\left(\frac{1}{\alpha_{\mathrm{it,j}}\sqrt{F_{\mathrm{it},j}}}\right)\right]^2}, \tag{43}$$

where the error combination function, E_j, is given by Equation (40).

Hence we have a quadrature summation of the photon errors due to the star and reference components of the combined star/iodine data, each being the weighted expected error in velocity across the respective template spectra scaled to the flux level of the data. As one would expect, the error goes with the inverse root of the mean flux in the data spectrum, $\left(\overline{F}_{\mathrm{m}}\right)^{-1/2}$; the error in each of the two components will also scale as the inverse of the visibility in the respective fringing spectra. Written in this form, the $E(\ldots)$ terms need only be calculated once, representing photon errors for each template: they then can be conveniently scaled and combined to give the error in each data frame for the source.

We note that these formulae for the photon limit are for the values expected *given* the fringe visibility that was obtained. Various instrument effects—for example, defocus, or a non-optimal delay for the stellar line width—can reduce the visibility from its optimum and hence reduce this photon limiting precision.

This has been the formalism employed in calculating the photon error for the Kitt Peak single-object ET for operations with an in-beam iodine cell. As an example, an observation taken at very high flux with the KPNO 2.1 m ET run in 2007 May of 36 UMa (stable, $V = 4.84$ mag, 10 minute exposure) gives mean S/N per pixel for star template, iodine template, and data frame of 222, 146, and 179 respectively. These values give photon errors for the star and iodine components of 2.8 and 1.5 m s^{-1} respectively, which when added in quadrature give a total photon error of 3.2 m s^{-1}. The KPNO instrument design is such that both output beams from the Michelson interferometer are recovered, and this result is for only one of the two beams. Averaging over the two beams therefore in fact gives a further improvement of $1/\sqrt{2}$ in photon precision; for simplicity, and for comparison with the following sections, we consider only one beam here, however. It is interesting to note that the error due to the iodine reference is in fact comparable in magnitude to that due to the star, since the signal in the iodine component of the data frame is intrinsically limited by the magnitude of the target being observed. Figure 4 shows a comparison of the actual rms (on the very short term) with the calculated photon errors using this formalism, obtained with the KPNO ET on the bright stable star 36 UMa over a total of ~2 hr, showing good agreement. The preceding example calculation is based on a data point at the high-flux end of this data set. (For the purposes of the plot, the two interferometer output beams are averaged.)

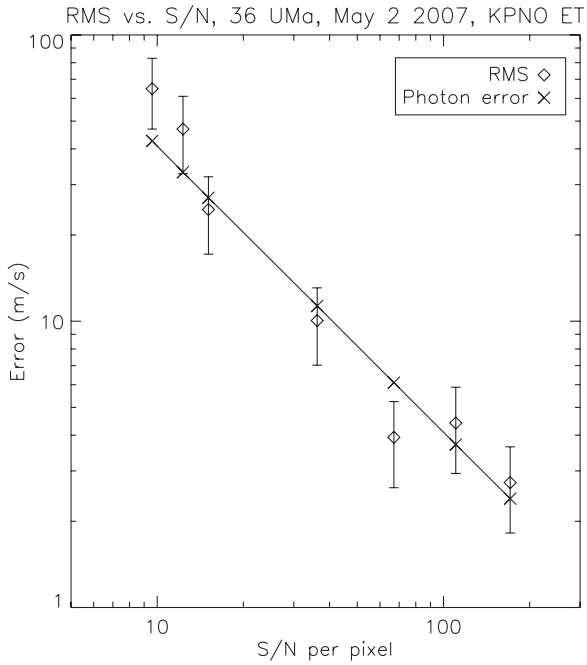

Figure 4. Measured rms vs. S/N per pixel for the bright stable star 36 UMa over a total of approximately 2 hr. Obtained with the KPNO ET on 2007 May 2, with varying exposure length to achieve different S/N levels, (approx. 5–6 data points per S/N level). Diamonds indicate the rms, with error bars corresponding to the uncertainty due to the number of data points over which the rms is calculated. Crosses and line indicate the corresponding calculated photon limit.

These calculations assume that the flux ratio terms remain the same from channel to channel, so that an overall mean scaling can be applied. This is not strictly accurate (e.g., if line depths are very deep and broad, or the pure star and pure iodine continuum functions are very different), but is taken to work to a reasonable approximation, and seems to correspond quite well with real results. In the event that a more accurate calculation is needed, however, it is a simple enough matter to introduce channel-dependent flux ratios for each element j within the summations.

3.1.2. Photon Error for Added-reference Spectrum

In the case of the reference spectrum being combined additively, rather than multiplicatively, the photon errors must be calculated differently. However, we can follow a somewhat

similar approach. Again, we consider the errors due to star and iodine components of the combined star/iodine data, and neglect the errors due to the templates, so that, as for Equation (41):

$$\varepsilon_v^2 = [E_j(\varepsilon_{v,\mathrm{sm},j})]^2 + [E_j(\varepsilon_{v,\mathrm{im},j})]^2, \tag{44}$$

where E_j is again defined as in Equation (40). The individual components $\varepsilon_{v,\mathrm{sm},j}$ and $\varepsilon_{v,\mathrm{im},j}$ must be reevaluated, however, since the photon noise from the two separate sources will now combine additively (for example, if one of the sources is considerably brighter than the second, its photon noise will dominate over the signal in the second). We can think of an effective visibility for the two components in the combined data, $\alpha_{\mathrm{sm},j}$ and $\alpha_{\mathrm{im},j}$. Remembering that fringe amplitude is given by the product of the visibility and the mean flux in the fringe, we can write

$$\alpha_{\mathrm{sm},j}\overline{F_{\mathrm{m},j}} = \alpha_{\mathrm{st},j}A_\mathrm{s}\overline{F_{\mathrm{st},j}}; \quad \alpha_{\mathrm{im},j}\overline{F_{\mathrm{m},j}} = \alpha_{\mathrm{it},j}A_\mathrm{i}\overline{F_{\mathrm{it},j}}, \tag{45}$$

where $\alpha_{\mathrm{st},j}$ and $\alpha_{\mathrm{it},j}$ are the fringe visibilities for channel j in the star and iodine templates respectively; and $\overline{F_{\mathrm{st},j}}$, $\overline{F_{\mathrm{it},j}}$, and $\overline{F_{\mathrm{m},j}}$ are the mean fluxes across the channel for the star template, iodine template, and data (measurement) frame, respectively. A_s and A_i are wavelength-independent scaling factors that allow for flux differences between the templates and the respective data components, as in Section 2.6.2. Hence we find

$$\alpha_{\mathrm{sm},j} = \frac{\alpha_{\mathrm{st},j}A_\mathrm{s}F_{\mathrm{st},j}}{F_{\mathrm{m},j}}; \quad \alpha_{\mathrm{im},j} = \frac{\alpha_{\mathrm{it},j}A_\mathrm{i}F_{\mathrm{it},j}}{F_{\mathrm{m},j}}, \tag{46}$$

where $F_{\mathrm{st},j}$ and $F_{\mathrm{it},j}$ are the total fluxes across the channel for the star and iodine templates, and $F_{\mathrm{m},j}$ is the total flux in the channel for the data frame. Substituting these effective visibilities in Equation (34) gives

$$\begin{aligned}\varepsilon_{v,\mathrm{sm},j} &= \Gamma\sqrt{2}\,\frac{\sqrt{F_{\mathrm{m},j}}}{\alpha_{\mathrm{st},j}A_\mathrm{s}F_{\mathrm{st},j}}\\ \varepsilon_{v,\mathrm{im},j} &= \Gamma\sqrt{2}\,\frac{\sqrt{F_{\mathrm{m},j}}}{\alpha_{\mathrm{it},j}A_\mathrm{i}F_{\mathrm{it},j}}.\end{aligned} \tag{47}$$

Using these we can now evaluate Equation (44) to obtain an estimate of the photon limiting error, so that

$$\varepsilon_v = \Gamma\sqrt{2}\sqrt{\left[E_j\left(\frac{\sqrt{F_{\mathrm{m},j}}}{\alpha_{\mathrm{st},j}A_\mathrm{s}F_{\mathrm{st},j}}\right)\right]^2 + \left[E_j\left(\frac{\sqrt{F_{\mathrm{m},j}}}{\alpha_{\mathrm{it},j}A_\mathrm{i}F_{\mathrm{it},j}}\right)\right]^2}, \tag{48}$$

where, due to flux conservation, A_s and A_i are subject to the constraint:

$$A_\mathrm{s}F_{\mathrm{st},j} + A_\mathrm{i}F_{\mathrm{it},j} = F_{\mathrm{m},j}. \tag{49}$$

Again we have found a quadrature summation of errors due to the star and reference components, scaled to match the respective component fluxes in the data, very similar to Equation (43). However, in this case, the scaling factors, A_s and A_i, must be determined as parameters during the velocity shift solution, and $A_\mathrm{s}F_{\mathrm{st},j}$ and $A_\mathrm{i}F_{\mathrm{it},j}$ represent the fluxes in the star and iodine components of the data, respectively.

This time, we do not attempt to assume channel-independent flux ratios. This is because for additively combined references it becomes possible to consider using emission spectra (e.g., a ThAr lamp) as the reference, rather than the usual iodine absorption spectrum. Clearly the flux ratio between data and reference template frames is very different for regions where there are no reference emission lines compared with those where emission lines are present. It is therefore not reasonable to take the flux terms outside the summation in the error combination function E_j.

To gain a handle on the behavior of Equation (48), we can see that if we consider only a single channel, so that for a function f, $E(f) \to f$, and assume both that the source and reference visibilities are roughly equal (reasonable for star and iodine, to order of magnitude) and that the total flux F_m remains constant, then to minimize the total error, we need only to minimize the function: $(A_\mathrm{s}F_{\mathrm{st},j})^{-2} + (A_\mathrm{i}F_{\mathrm{it},j})^{-2}$. Given the constraint of Equation (49) it is straightforward to show that this is minimized when $A_\mathrm{s}F_{\mathrm{st},j} = A_\mathrm{i}F_{\mathrm{it},j}$, in other words, when the component star and iodine fluxes are approximately equal. When either component has a very small flux compared with the other, one or other of the terms in Equation (48) will become very large. Broadly speaking, then, we can see that the fluxes of star and reference need to be balanced in order to minimize photon error.

In practice, rather than the total flux being constant, it is of more interest to hold the stellar component constant and vary the reference component to find the optimum; using real spectra, and allowing differing visibilities, the balance point becomes a little skewed from unity. The exact optimal balance point depends on the spectra in question. Allowing for the gain in optical throughput from losing the absorption in the gas cell reference, this equation at its balance point generally gives photon errors on a similar level to the photon errors for a multiplied iodine reference, if we use iodine spectra as references in both cases (i.e., tungsten-illuminated iodine in the added-reference scheme). Using the same observations as in Section 3.1.1 to calculate error estimates as if the spectra had been added, and assuming that the flux level of the star in the template and the hypothetical combined observation is the same, we find an optimal ratio of iodine to star flux of 0.96 and a total photon error of 3.6 m s^{-1}, comprised of iodine and star component errors of 3.1 m s^{-1} and 1.8 m s^{-1}, compared to the total error of 3.2 m s^{-1} for multiplied spectra. That the two are similar is not surprising: adding a reference spectrum to the stellar spectrum at a matching flux level will approximately halve fringe visibility and hence double the error, but also double the flux, reducing the error by $1/\sqrt{2}$, giving a total $\sqrt{2}$ increase in the error size. This coincidentally matches the increase in error size for in-beam-iodine calibration due to the fact that the iodine typically absorbs ~50% of the incident light. (The slight mismatch in the figures calculated is due to the fact that in the multiplicative case, the combined data frame actually had particularly high flux, probably because of better sky transparency at the time the frame was taken than when the template was taken).

The above argument holds true for iodine since the continuum shape and fringe visibilities are broadly similar to those of the stellar spectrum. If we instead use a ThAr emission spectrum for the added reference, we appear to perform even rather better than the in-beam iodine case: the same calculations as above with a ThAr spectrum replacing the iodine spectrum yield a total photon error of 2.5 m s^{-1}, with star and ThAr components of 2.4 m s^{-1} and 0.65 m s^{-1} respectively (with an optimum ratio of mean fluxes of 0.26—now substantially different because of the very different nature of an emission spectrum). ThAr also shows a weaker dependence on relative flux level, which gives it an advantage in terms of practical application since less effort would need to be expended on matching the brightness to each

target observation. This is likely because most of the Doppler information is primarily concentrated in a few bright lines in the ThAr, where it is spread more broadly across the stellar spectrum. Where the ThAr lines are strong, the stellar Doppler information is likely largely lost due to the added photon noise. However, since there are relatively few such lines, there is not too much impact on the total stellar Doppler information, and increasing the ThAr flux does not make as large a difference as for the case of an iodine spectrum. We note, however, that at very high flux levels, saturation of the brightest ThAr emission lines is likely to complicate this analysis somewhat.

Added-beam reference calibration provides one possible solution to the reference addition approximation error discussed in Section 3.3.3, and the discussion here should provide a formalism for calculating the photon errors. Such a calibration approach, however, has not yet been attempted within the ET program, although basic simulations bear out these calculations.

3.1.3. Photon Error with a Separate Reference

Finally we consider the simple case where there is no simultaneous common-path reference, but rather a reference separated either spatially or in time. Once again, we find a weighted mean velocity shift between (now pure) star measurement and some reference star template, and the same between a pure reference spectrum measurement and a corresponding template. (The reference need not be iodine, but we retain the "i" subscript notation for consistency). The results are differenced to obtain a corrected intrinsic stellar Doppler shift. If we neglect the template errors as before, then the photon errors for the data frame are found again similarly to Equation (41):

$$\varepsilon_v^2 = [E_j(\varepsilon_{v,\mathrm{s},j})]^2 + [E_j(\varepsilon_{v,\mathrm{i},j})]^2. \tag{50}$$

The difference is that here we use subscripts "s" and "i," rather than "sm" and "im," to indicate that we are no longer looking at components of a combined reference/star measurement frame, but at pure star and pure reference measurements, respectively. Again substituting the basic photon error Equation (34), we obtain

$$\varepsilon_v = \Gamma\sqrt{2}\sqrt{\left[E_j\left(\frac{1}{\alpha_{\mathrm{s},j}\sqrt{F_{\mathrm{s},j}}}\right)\right]^2 + \left[E_j\left(\frac{1}{\alpha_{\mathrm{i,j}}\sqrt{F_{\mathrm{i},j}}}\right)\right]^2}. \tag{51}$$

The form of the equation is now much simpler, since no flux or visibility scaling is required. Errors again go as the inverse of the visibilities of star and iodine, and as the inverse root of the flux. It may also be the case (indeed, observations should be taken such that it is the case) that the reference spectrum has significantly higher S/N, and therefore its photon errors can be neglected, so that only the first error combination term in the square root remains.

Taking our same data and templates once again, we can calculate a hypothetical photon error for comparison: this time, using iodine as a separate reference yields a total error of 2.9 m s^{-1} comprising star and iodine components of 2.3 m s^{-1} and 1.9 m s^{-1} respectively (note that the iodine error level here is relatively high in comparison to the star component: this is purely because of the exceptionally high flux from the star in these particular observations); using ThAr instead yields a total error of 2.4 m s^{-1}, with star and ThAr components of 2.3 m s^{-1} and 0.77 m s^{-1} (though again we have not included the effects of saturation in the ThAr calculation, which may increase the ThAr errors somewhat).

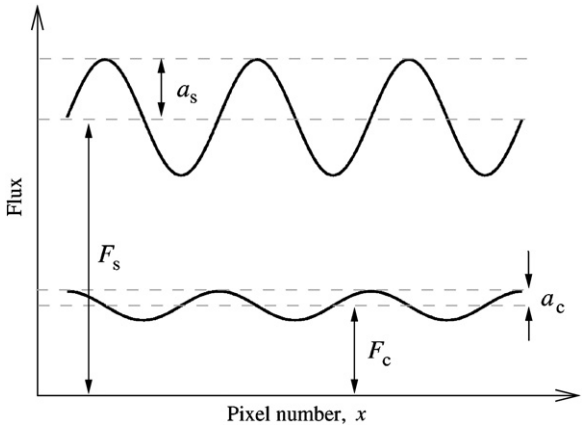

Figure 5. Fringe along one channel due to source (upper curve) and contaminating low flux fringe (lower curve). Measured fringe is a summation of these two fringes.

This approach is appropriate to the MARVELS/Keck ET, where pure star science exposures are bracketed in time with pure iodine reference exposures, and the instrument is highly stabilized in both pressure and temperature. The baseline design requirements anticipate a photon error of 3.5 m s^{-1} at V = 8 mag, and 21.5 m s^{-1} at V = 12 mag (see Section 4.4 and Ge et al. 2009).

3.2. Additive Contaminating Spectra

It is often useful to be able to calculate a rough estimate of the errors due to contaminating additive background spectra. We derive a formalism for doing so here. This formalism will enable us to calculate the effect of background moonlight contamination, contaminating background stars, or double-lined spectroscopic binaries, for example. In addition, we will then be able to extend the formalism to treat multiplicative (i.e., flux independent) contaminants, such as any residual unfiltered comb presence or the iodine/star cross-talk term that causes the reference addition approximation error, and try to assess their relative significance.

3.2.1. Derivation

Figure 5 shows a fringe along one detector column (in the slit direction) due to the target source alone, with fringe amplitude a_s, mean flux F_s, and phase ϕ_s. For simplicity we assume no iodine fiducial reference, since we are only aiming for an order-of-magnitude estimate. A second contaminating fringe of lower amplitude a_c and mean flux F_c due to background contamination is also shown, with phase ϕ_c. If the spatial frequency of the fringes is f, then the summation of these two fringes will give the total (also sinusoidal) measured fringe:

$$\begin{aligned} &F_s + \Re\{a_s e^{i(fx+\phi_s)}\} + F_c + \Re\{a_c e^{i(fx+\phi_c)}\} \\ &\quad = F_s + F_c + \Re\{a_s e^{i(fx+\phi_s)} + a_c e^{i(fx+\phi_c)}\}, \end{aligned} \tag{52}$$

where x identifies position along the slit. $F_s + F_c$ represents the mean value of the measured flux. The last term represents the varying sinusoidal net fringe.

We are interested in the phase error, ε_ϕ, introduced into the measured fringe by the contaminating spectrum. Since we are only interested in the phase information, we ignore the offset term $F_s + F_c$, and represent the varying term as a vector summation, as shown in Figure 6, where a_s and a_c represent the source and contaminant fringe amplitudes as before. The

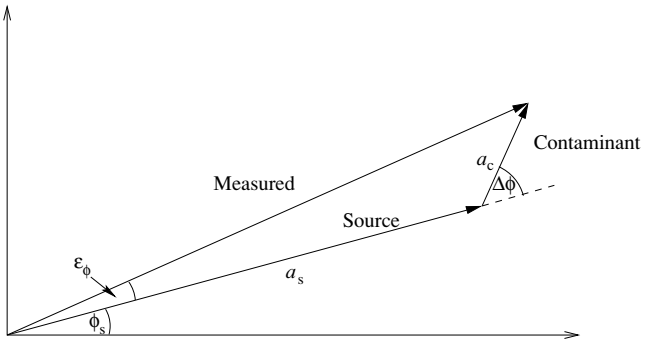

Figure 6. Vector representation of the summation of the fringes due to the target source and background contamination.

angle $\Delta\phi$ is the difference between the source and contaminant fringe phases, $\Delta\phi = \phi_c - \phi_s$. Using the sine and cosine rules for triangles we can show

$$\frac{\sin\varepsilon_\phi}{a_c} = \frac{\sin\Delta\phi}{\sqrt{a_s^2 + a_c^2 + 2a_s a_c\cos\Delta\phi}}. \quad (53)$$

First we consider the case that the two spectra are of *similar form* and *very close in velocity*, so that $\Delta\phi$ is small. Then,

$$\sin\varepsilon_\phi \approx \frac{a_c\Delta\phi}{a_s + a_c}. \quad (54)$$

If we assume the source and contaminant fringe visibilities are approximately equal, so that $a_s/F_s \approx a_c/F_c$, then $a_c/a_s \approx F_c/F_s$, which is equal to the flux ratio of the two fringes. If the contaminating fringe is much fainter than the source, so that $F_s \gg F_c$, therefore $a_s \gg a_c$, and hence ε_ϕ is small, then

$$\sin\varepsilon_\phi \approx \varepsilon_\phi \approx \frac{a_c}{a_s}\Delta\phi = \frac{F_c}{F_s}\Delta\phi. \quad (55)$$

Still assuming that the two spectra are of similar type and velocity, then all wavelength channels will see approximately the same phase difference between source and contaminant fringes, and this error will be systematically close to the same across all channels. Therefore, the same result will be expected finally even after averaging over all channels. Since $\Delta\phi$ is proportional to the difference in velocity, Δv, between source and contaminant, then we can write the final error in the measured velocity, ε_v, simply as

$$\varepsilon_v \approx \overline{(F_c/F_s)}\Delta v \approx \frac{\overline{F_c}}{\overline{F_s}}\Delta v, \quad (56)$$

where now $\overline{F_c}$ and $\overline{F_s}$ signify mean fluxes for the entire spectra, rather than for individual channels. In other words, the systematic velocity error due to a faint contaminant of similar spectral type that is closely matched in velocity is simply the velocity difference scaled by the flux ratio of the contaminant to the source fringe. (The approximation made in dividing the means in the second form of this equation is good to first order, and provides a very convenient way to quickly estimate the errors. See Appendix C for a derivation and discussion of when it is more appropriate to use the first form of the equation. The same approximation is also made use of several times below.)

This relation does not hold well to arbitrarily large velocity differences, however. From the geometry of Figure 6 it can be seen that a worst case scenario is where the contaminant in all channels is systematically offset by an amount such that the background contaminant vector is perpendicular to the measured vector (or, approximately, where $\Delta\phi = \pi/2$). In this case, $\varepsilon_\phi \approx a_c/a_s \approx F_c/F_s$, so that

$$\varepsilon_v \approx \Gamma\frac{\overline{F_c}}{\overline{F_s}}, \quad (57)$$

where Γ is the phase/velocity scaling factor. Hence the "worst case scenario" error, where the velocity offset between source and contaminant is the worst possible and the two spectra are very close in form, is again simply proportional to the contaminant-to-source flux ratio.

In the limit that the spectra are completely *dissimilar*, or are sufficiently separated in velocity space that overlapping features are in no way correlated, then the phase errors will be randomly distributed across all channels. Following again from Equation (53), we once again assume $F_s \gg F_c$ and $a_s \gg a_c$, which allows us to neglect the a_c^2 and $\cos\Delta\phi$ terms; and again that on average $a_s/F_s \approx a_c/F_c \Rightarrow a_c/a_s \approx F_c/F_s$. Now, however, taking $\Delta\phi$ as uniformly randomly distributed, we can find the rms value for the phase error in one channel as

$$\mathrm{rms}(\sin\varepsilon_\phi) \approx \mathrm{rms}(\varepsilon_\phi) \approx \mathrm{rms}\left(\frac{a_c}{a_s}\sin\Delta\phi\right) = \frac{F_c}{F_s}\frac{1}{\sqrt{2}}. \quad (58)$$

Assuming an average over n independent channels gives a $1/\sqrt{n}$ reduction in the final error, so that for uncorrelated spectra, we can expect a final velocity error of

$$\varepsilon_v \approx \frac{\Gamma}{\sqrt{2n}}\frac{\overline{F_c}}{\overline{F_s}}, \quad (59)$$

where Γ is the phase–velocity scale factor for the instrument. The error is now independent of differential velocity between source and contaminating spectra, since the two spectra no longer bear any relation to each other (although it may be expected to vary systematically on velocity difference scales corresponding to the line widths).

3.2.2. Application to Moonlight and Stellar Contamination

Equations (56), (57), and (59) can be applied directly to estimate the magnitude of the errors introduced by background-scattered moonlight contamination. As an example, a 3″ fiber with a bright-time sky background of 19 mag arcsec^{-2} due to scattered moonlight from the atmosphere gives a total of 16.9 mag of sky background. For a magnitude 12 star, this gives a source-to-contamination flux ratio of about 90. In the worst case scenario, from Equation (57), assuming $\Gamma \sim 3700$ m s^{-1} rad^{-1} (corresponding to a 7 mm delay), we find $\varepsilon_v \approx 41$ m s^{-1}. This will apply where the stellar spectrum is similar to the moonlight spectrum (not uncommon, since most targets are sun-like), and in the case where the velocity difference between star and moonlight, Δv, is coincidentally around ~6 km s^{-1}. At smaller velocity differences, the error will scale roughly linearly as $\varepsilon_v = \Delta v/90$ up to this point (Equation (56)). After that, it will improve again as $\Delta\phi$ increases to π, where the phase error once again approaches zero. As $\Delta\phi$ increases, the behavior is likely to be somewhat oscillatory, with a period of $2\pi\Gamma = 2.3 \times 10^4$ m s^{-1} owing to the geometry of Figure 6, decaying until Δv is large enough that the two spectra are completely uncorrelated. For $n = 1000$ *independent* wavelength channels (i.e., 4000 pixel channels with an LSF

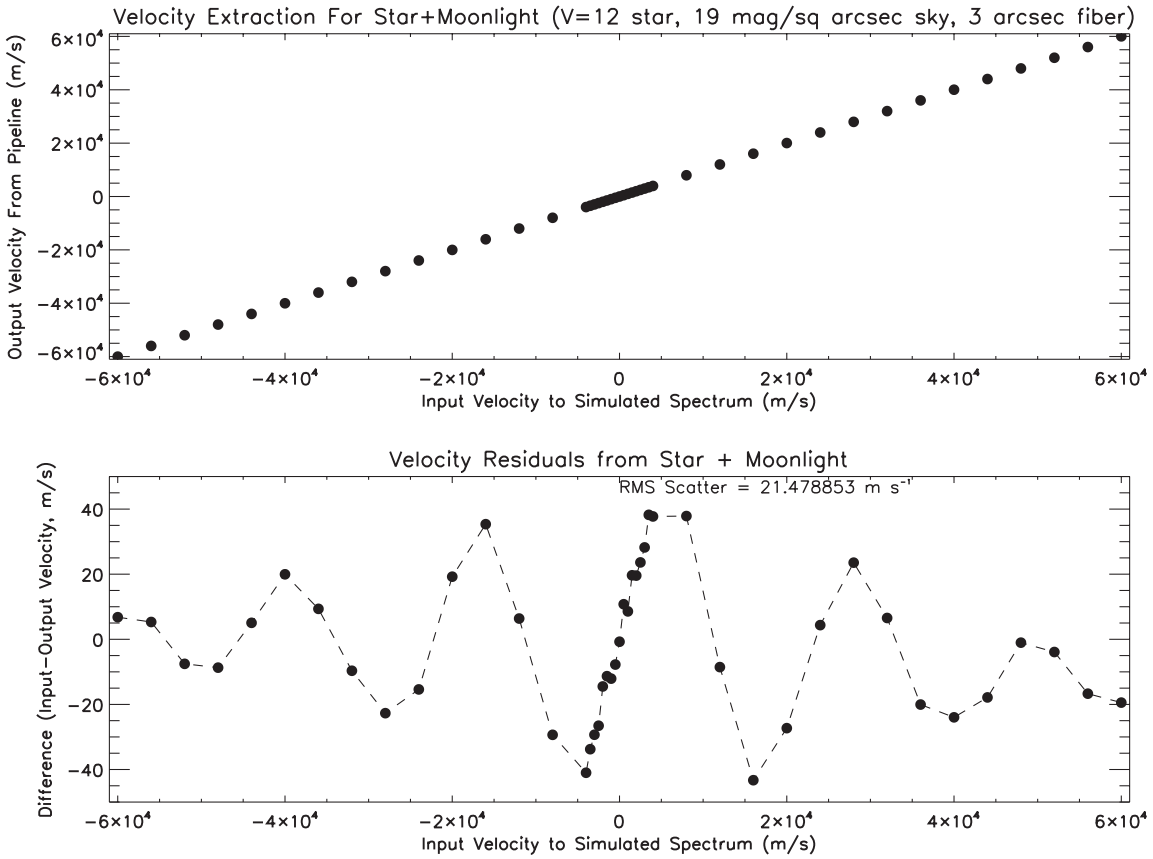

Figure 7. Simulations of moonlight contamination, showing the systematic error introduced by contaminating moonlight at 19 mag arcsec^{-2} for a $V = 12$ F9V star on a 3″ fiber, as a function of velocity difference between target star and moon spectrum.

∼4 pixels wide), the error should then approach Equation (59), with an rms value of around $\varepsilon_v \approx 0.8$ m s^{-1}. This should also be the typical error size when the star and moon spectra are very different in form.

Simulations of the effect of moonlight contamination show reasonable agreement: Figure 7 shows the RV deviation caused by synthetic moonlight contamination added to a synthetic stellar spectrum, and then multiplied by the interferometer response function and degraded in resolution to simulate real instrument spectra (ignoring the iodine reference). The resulting spectra are run through the standard ET reduction pipeline to assess the effects of the contamination.

The instrument parameters given here are chosen to match the parameters of the simulation, which reflect a typical ET-like instrument design. For comparison, the MARVELS/Keck ET in fact uses 1.″8 fibers, with $\Gamma \sim 3400$ m s^{-1} rad^{-1}, leading to a worst-case error of only 14 m s^{-1}, at the faintest end of the MARVELS range. Reducing the fiber size is clearly one effective way of mitigating the effect of moonlight contamination, although this may be at the expense of throughput if telescope guiding or seeing is not optimal. Reduction of moon contamination error is discussed further in Section 4.1.

In exactly the same way, we can calculate the effects of contamination by a background star: for example, a background star of the same spectral type and class, but 5 mag fainter (i.e., fainter by a flux ratio of 100) would give about the same level of error. At increasingly different spectral types, the contaminant star will cause less of a problem as the spectra become less correlated. Hence for a faint companion (as opposed to background) star, although the flux ratio may be higher, the effect will be at least partially mitigated by the difference in spectral type.

3.3. Multiplicative Fringe Contamination

In addition to additive contaminating spectra, certain errors can appear as multiplicative effects in the fringing spectra. These are independent of flux and correspond more closely to fringe errors rather than flux errors in the spectra. Residual interferometer comb, for example, will behave in this way (a concern for multiplied-reference modes of operation), and the cross-talk term from the reference addition approximation can also be considered in the same way.

3.3.1. Derivation

We can follow the same formalism as for background spectrum contamination. In this case, however, instead of the source and contaminant fringe *visibilities* being similar, the fluxes are similar, so that $F_s \approx F_c$. Dividing the denominators of Equation (53) through by $F_s \approx F_c$, we can replace the fringe amplitudes a_s and a_c with their respective visibilities $\alpha_s \equiv a_s/F_s$ and $\alpha_c \equiv a_c/F_c$. The source spectrum and interferometer comb are completely unrelated in form. Assuming $\alpha_c \ll \alpha_s$ we can follow the same reasoning as for Equation (59) and write

$$\varepsilon_v \approx \frac{\Gamma}{\sqrt{2n}} \frac{\overline{\alpha_c}}{\overline{\alpha_s}}, \tag{60}$$

where $\overline{\alpha_c}$ and $\overline{\alpha_s}$ are representative visibilities for the entire contaminant and source spectra respectively (again see Appendix C

regarding the division of means here). The error is now proportional to the ratio of visibilities, and again decreases with the root of the number of spectral channels, n.

3.3.2. Application to Residual Interferometer Comb

As an example application, we can consider the effect of residual interferometer comb. For the case of using a multiplied fiducial spectrum such as in-beam iodine absorption, if the interferometer comb (Section 2.4) is not completely removed—either by careful tuning of interferometer delay and slit width or by Fourier filtering in the data processing—then it acts as contaminating fringes. In order for the reference addition approximation to work, the comb term in Equation (22) must be completely removed (see the subsequent discussion). This has in the past been an issue with some configurations of the ET instruments, for example: in these cases the sampling by the resolution element was such that the comb was aliased in places, creating a low-frequency pattern in the dispersion direction which was impossible to filter out without losing significant Doppler information.

Here, it is appropriate to take the combined star/iodine data as the source spectrum, since the comb error arises in the formula for the combined data (Equation (22)). A residual comb visibility of 0.5% (cf. ∼1% comb visibility in unfiltered KPNO ET data) on top of a spectrum of typical mean visibility of say, 4%, and taking the KPNO ET value of $\Gamma \sim 3300$ m s^{-1} rad^{-1} with $n = 1000$ independent channels, would give an expected error of $\varepsilon_v \approx 9$ m s^{-1}.

In practice, however, we have found that, provided comb aliasing is avoided in the instrument design and alignment, removing the interferometer comb during image preprocessing with a simple one-dimensional low-pass Fourier filter appears to be effective in completely mitigating this error. The comb cannot be measured or seen by eye above the photon noise in filtered continuum lamp spectra, and we have not yet found any evidence of residual comb causing problems in the final data.

3.3.3. Application to the Addition Approximation

In order to estimate the errors introduced by the addition approximation discussed in Section 2.6.1, we can also follow a similar approach, treating the cross term from Equation (22) which is ignored in the approximation (or rather, treating the *lack* of cross term) as if it were a contaminating spectrum. First, we consider the simplified case of two discrete overlapping Gaussian absorption lines, from template spectra labeled A and B (e.g., an iodine and a stellar line), combined by multiplication to give the measured spectrum, labeled M. Both line centers are exactly coincident. The fractional line depths are represented by D ($0 \leqslant D \leqslant 1$), with corresponding subscripts a, b, and m. From Ge (2002), we have that in general

$$\alpha = De^{-3.56d^2/l_c^2} \equiv KD, \tag{61}$$

where α is the absolute fringe visibility (so that the complex visibility is $\boldsymbol{\alpha} = \alpha e^{i\phi}$ as usual), d is the interferometer delay, $l_c = \lambda^2/\Delta\lambda$ is the coherence length of the interferometer beam with line width $\Delta\lambda$ at wavelength λ, and $K = \exp(-3.56d^2/l_c^2)$ is a constant (for a given wavelength). Although not very realistic, we begin by assuming both lines A and B and the resulting line M are of similar width, and that the measured line, which is the product of the two lines, is also approximately Gaussian. K is then approximately the same for all three lines.

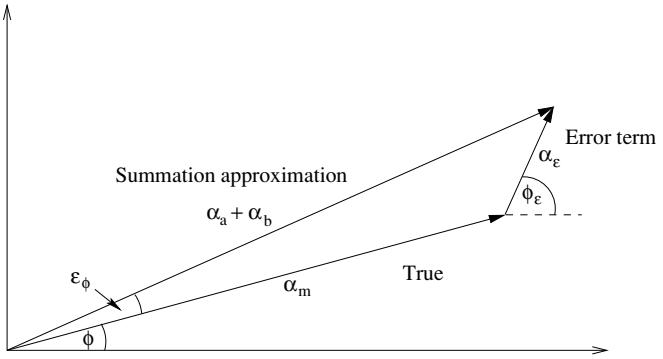

Figure 8. Vector representation of the summation of the true complex visibility and the error term due to the addition approximation.

We can then write

$$\begin{aligned}\alpha_m &\approx D_m K = [1 - (1 - D_a)(1 - D_b)]K \\ &= [D_a + D_b - D_a D_b]K \\ &= \alpha_a + \alpha_b - D_a D_b K. \end{aligned} \tag{62}$$

In the addition approximation, the complex visibilities of the template spectra are added together. In this simple case, the two lines are centered at the same wavelength and both are Gaussian, so that one line is simply a scaled version of the other. By the linearity of Fourier transforms, this means that the phases of the two complex visibilities must be identical, so that in the addition approximation, the two absolute visibilities add to give $\alpha_m \approx \alpha_a + \alpha_b$. The remaining term in Equation (62) is therefore approximately the error, α_ε, the difference between the added templates and the actual measured visibility:

$$\alpha_\varepsilon = D_a D_b K. \tag{63}$$

In the more general case that the two line centers are not exactly coincident or the same shape, so that the respective template fringes are not in phase, the error term will also include a phase difference, becoming a two-dimensional vector, $\alpha_\varepsilon e^{i\phi_\varepsilon}$. Taking the error term above as a reasonable estimate of the length of this vector and assuming ϕ_ε is uniformly randomly distributed, we can calculate a corresponding representative error in phase of the summation approximation. Figure 8 shows the addition of the "true" (measured) complex visibility and the error term to give the solution according to the summation approximation. ϕ represents the phase of the true complex visibility, and ε_ϕ represents the error in the measurement of that phase. If we assume the resulting measured visibility vectors and the error terms are uncorrelated from channel to channel, and if we take D_a and D_b to be some kind of representative average line depth for the two spectra across all j, we can derive the typical expected velocity error following the same reasoning as for Equation (60) and write

$$\begin{aligned}\varepsilon_v &= \frac{\Gamma}{\sqrt{2n}} \frac{\alpha_\varepsilon}{\alpha_m} \\ &= \frac{\Gamma}{\sqrt{2n}} \frac{D_a D_b}{D_a + D_b - D_a D_b}, \end{aligned} \tag{64}$$

where n is again the number of independent channels, and the constant K cancels. (Note that although angles ϕ_ε in Figure 8 and $\Delta\phi$ in Figure 6 are measured from different origins, they are in both cases taken to be uniformly randomly distributed between 0 and 2π, so that the same reasoning applies for both.)

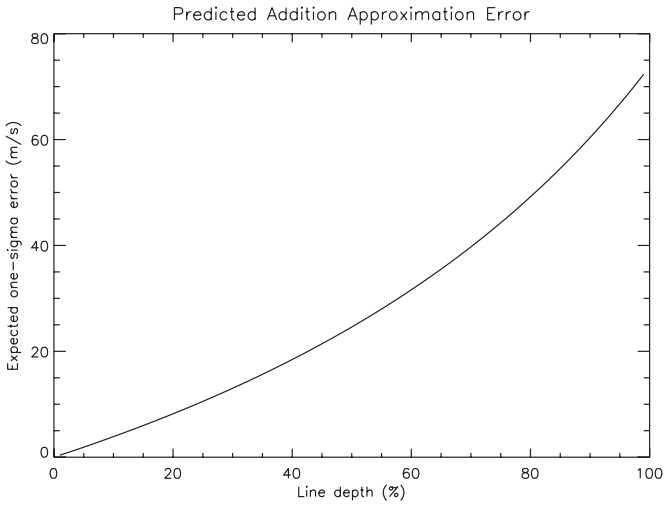

Figure 9. Analytically calculated expected error due to the addition approximation, assuming approximately equal line depths for both star and reference spectra.

Hence we find again that the error decreases as the square root of the number of spectral channels; unsurprisingly, it also increases with line depth, since deeper lines allow for more cross talk. If, however, either one of the representative line depths is very small, then the velocity error also becomes small, becoming approximately linear with the smaller line depth and independent of the larger as the smaller tends to zero.

Figure 9 shows the expected typical error as a function of average line depth for the simplified case where the typical depths of the two spectra are equal, and taking $\Gamma \sim 3300$ m s^{-1} rad^{-1} and $n = 1000$. For average line depths of, say, 80% for both star and iodine, this gives a typical error due to the addition approximation of $\sim$50 m s^{-1}, which is clearly very significant. The error will manifest as a systematic error in the velocity response of the instrument, essentially adding noise which varies as a function of the specific overlapping of the lines between target star and reference spectrum. It will therefore vary with stellar spectral type, class, and line width, and will also vary as a function of the intrinsic absolute Doppler shift of the stellar spectrum. Since the stellar lines are generally considerably broader than the iodine lines, if the stellar lines slowly shift relative to the iodine lines, the noise term will slowly change until the point where a shift of more than a stellar line width has been reached. At this point, the stellar lines are overlapping completely new iodine features, and the noise term will take on a new value that is completely uncorrelated with its previous value. Hence, we expect a nonlinearity in the velocity response of the instrument, with a standard deviation somewhere on the order of 50 m s^{-1} and that varies with Doppler shift on a scale of approximately the line width of the star. For solar-type stars observable with ET, this variation will be over scales typically on the order of 5–10 km s^{-1}.

Figure 10 shows the results of simulated fringing spectra run through the reduction pipeline to see the effect of nonlinearity due to the addition approximation, and shows broad agreement with these expectations. (For the simulation, the phase–velocity scaling factor $\Gamma \approx 3700$ m s^{-1} was used; for this value of Γ, our previous calculation yields $\sim$55 m s^{-1}.)

Clearly the addition approximation is a very significant source of systematic error, and cannot be neglected. The systematic error will affect any DFDI instrument that depends on in-beam multiplied reference spectra. Various approaches to correct the error are under consideration, although an exact analytical solution—if one exists—remains elusive; for the MARVELS survey and the current KPNO ET (now undergoing upgrade) simultaneous in-beam iodine calibration is simply avoided, instead relying on good instrument stability and bracketing exposures in time with reference iodine frames to calibrate out instrument drift. Possible approaches to dealing with the addition approximation error are discussed in Section 4.2, and alternative calibration methods that circumvent the approximation altogether in Section 4.3.

4. DISCUSSION

4.1. Moonlight Contamination

As surveying for exoplanets down to fainter and fainter magnitudes during bright-sky time continues with the MARVELS project, moonlight contamination is likely to become an important issue (keeping fiber diameter small and avoiding bright time notwithstanding). With the current ET instruments and pipeline, it is unlikely that direct subtraction at the whirl or the initial image stage would be successful. Bracketing science exposures in time with sky exposures to measure the background would seriously impact the observing cadence, reducing on-sky exposure time by a factor of 2 or more, and would likely suffer from rapidly varying sky background in the presence of even a thin cloud. Using simultaneous sky-fibers alongside the science fibers for direct subtraction in image space would require extremely precise modeling of the instrument to successfully map the spectrum from one fiber onto another. For subtraction in whirl space there is insufficient flux from such a faint background to be able to successfully measure meaningful whirls, at least using our current data analysis techniques.

Given adequate templates of the moon spectrum, however (a solar spectrum may suffice), then it may be possible to model out the moon error by treating it as a further additive component in solving for the stellar Doppler shift, just as for the case of added-reference spectra. This could in principle be done alongside any simultaneous reference spectra, and since the moon spectrum is an additive component, it would not suffer from the addition approximation errors associated with an in-beam calibration source. Alternatively, currently under consideration for reducing ET data, forward modeling from high-resolution spectra to match the measured whirl data (or even the fringing spectrum images) could allow for moon contamination to be included as a part of the model.

The original KPNO ET having been designed for brighter sources where moonlight is less of a concern, approaches to mitigation of moonlight contamination are still under investigation.

4.2. The Addition Approximation Error

One of the most significant concerns with the DFDI technique for exoplanet searches when using superposed iodine is clearly the addition approximation error. Causing long-term systematic errors on the scale of up to $\sim$100 m s^{-1}, the approximation can potentially have a serious adverse effect on the measurement of exoplanet RV signatures. The effect can be mitigated to a certain extent simply by judicious selection of observation times and positions of targets on the sky, so that the line-of-sight barycentric motion of the Earth—usually the dominant effect that causes the nonlinearity to become significant—is minimized. Such observations are often not hard to achieve at least over periods of a few days. This explains why we were

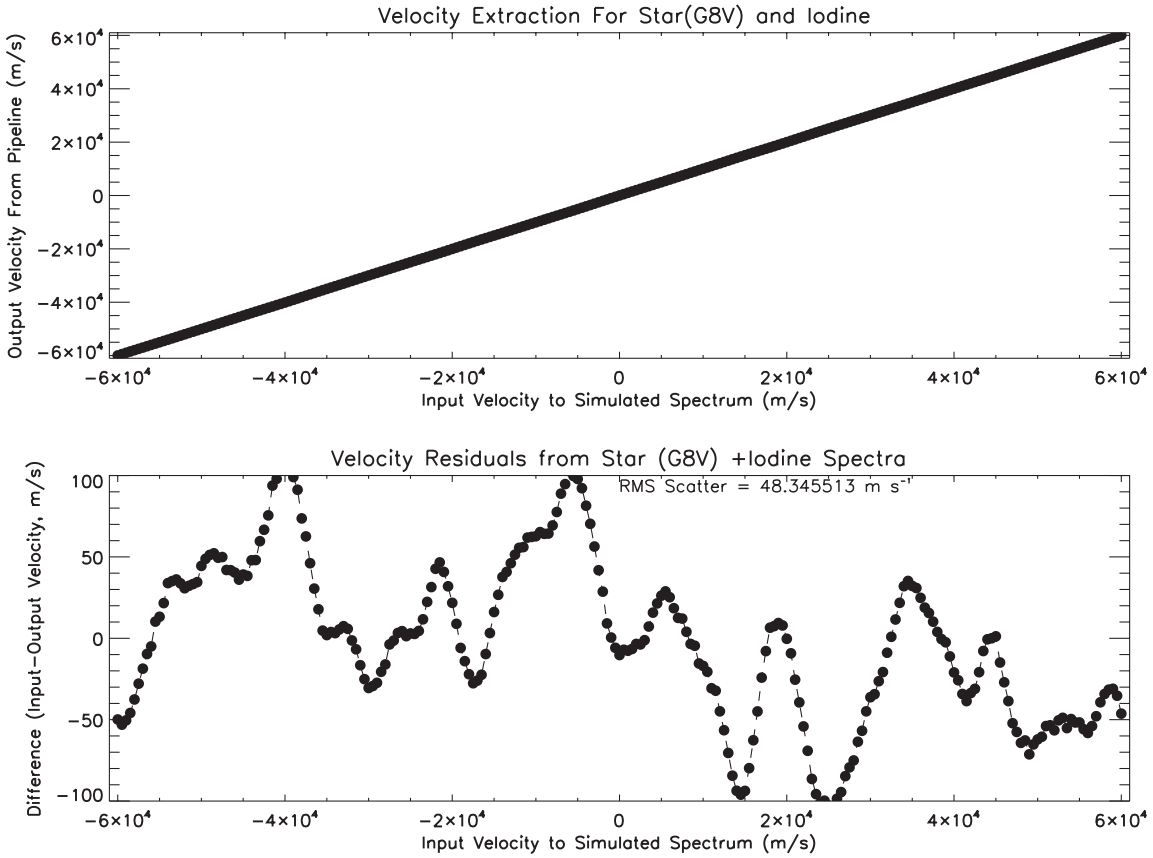

Figure 10. Simulations showing the addition approximation error. The nonlinearity in the RV response has the same order of magnitude and appears on the same input velocity scales as expected from theoretical predictions.

earlier still able to make successful detections of 51 Peg b and HD 102195 b (van Eyken et al. 2004a; Ge et al. 2006) despite then being unaware of the effect: for both targets, the sky positions and epochs of observation were such that the change in barycentric correction over the lengths of the individual observing runs was small compared to the variation scale of the addition error, so that the addition errors were absorbed in small corrections to the phase–velocity scale. Nonetheless, the addition approximation error becomes significant for velocity shifts on scales upward of the line width of the stellar spectrum, and placing stringent constraints on the times of observation is likely to cause serious aliasing issues due to the observation window function. Furthermore, over 24 hr, the barycentric motion of the observatory contributes a variation of up to $\sim$1 km s^{-1} in RV due to Earth's rotation, and up to 60 km s^{-1} over a year due to Earth's orbital motion. For the slowest rotating, most narrow-lined (and hence best Doppler precision) stars, the line width may be on the order of 1 km s^{-1}, so that even over one night the error is of concern. Forcing the observing cadence is therefore certainly not a satisfactory long-term solution.

Clearly, a robust solution to the problem of the addition approximation error needs to be found. The ideal would be to find a mathematically exact solution to the spectrum combination equations—or at least a more accurate approximation—but this remains elusive, and it is not clear whether such a solution even exists. Modifying the template whirls cannot solve the problem, since the templates themselves are correct: to solve the problem, the cross-talk term discussed in Section 2.6.1 that constitutes the error must be directly calculated, or at least approximated. Hence iterative approaches which perturb the template whirls in an attempt to minimize the residuals will only end up introducing error in order to fit the cross-talk term.

One way or another, calculating the cross-talk term seems to require knowledge of the underlying high-resolution spectrum of the two templates. Efforts to model the error term using high-resolution iodine and synthetic stellar spectra have shown some promise. In this approach, the cross-talk term is calculated directly, so that a grid of corrections across velocity and stellar parameter space can in principle be created to apply to real data. Alternatively, appropriately parameterized high-resolution spectra could be forward modeled to match the data from the instrument, using the formalisms previously presented: as well as accounting for the cross-talk term naturally as part of the process, this could also allow for addition of a third spectrum in the model to account for sky background in an attempt to remove moonlight contamination. This would, however, likely require extremely precise modeling and calibration of the instrument, losing the benefit of the self-calibrating nature of real templates.

Alternatively, one can consider trying to obtain the high-resolution information from the data itself. Two possible approaches to recreating the underlying spectrum are as follows: one is to begin with the low-resolution non-fringing spectra obtained from the DFDI fringing spectra (e.g., by binning the spectrum in the slit direction) as an approximation, using this to help model the cross talk, and then iterate with successive perturbations to the spectrum until the residuals between real data whirl and the sum of the template whirls and the cross-talk correction are minimized (similar to the approach by Johnson et al. 2006 used to measure RVs without formal templates using a traditional spectrograph). All the information necessary

to reconstruct the underlying spectrum may not be present in the cross-talk term, however: one can imagine degeneracies, for example, where two closely spaced absorption lines within a resolution element may lead to the same fringe phase and visibility as a single line of a different depth positioned midway between the two. It may therefore not be possible to iterate toward a single solution based on a single data frame. However, once multiple observations at different RVs have been taken, where the stellar lines overlap different parts of the reference spectrum, we might conceivably be able to use the aggregate information to help break any degeneracies. The more data measurements, the more accurate becomes the estimate of the underlying spectrum. This is somewhat analogous to the concept employed by Konacki et al. (2009) in improving individual star templates from double-lined spectroscopic binaries.

The second approach which is likely to be simpler is to try and obtain an improved estimate of the cross-talk term by calculating it based on template spectra reconstructed at higher resolution than the nominal spectrograph resolution by using the information in the fringes. Such a reconstruction is described by Erskine et al. (2003). Although having a single fixed delay constrains the degree to which high-resolution information can be recovered, it could at least provide a first-order correction for the addition approximation error.

At the time of writing, all these approaches represent avenues for further investigation; the best solution may involve some combination of the above.

4.3. Alternatives to Multiplied References

Instead of attempting to calculate or model the addition approximation error, an alternative is to circumvent the problem altogether by considering different instrumental approaches to RV calibration.

One such approach would be "combined beam" superposition of the reference spectrum, where a reference is literally added to the stellar spectrum, for example, by splicing two input fibers together into one. In this way, there is no longer an approximation in combining the template whirls: the equations are exact (Section 2.6.2). Combined-beam superposition does run the risk of adding photon noise to the stellar spectrum: for an absorption reference (e.g., a tungsten-illuminated iodine cell), the star and reference spectra need to be balanced in flux. This adds complexity to the observing in that it requires advance knowledge of target fluxes and careful preparation for observations, and is more likely to be practical for a single-object than a multi-object instrument. Calculations of the added-reference photon limit based on real KPNO ET fringing spectra suggest that provided the spectra are properly balanced, similar precision can be obtained as for a multiplied reference spectrum at a given S/N in the data, when one allows for the gain in flux from the lack of reference absorption. Similar test calculations with ThAr emission as a reference show that the photon noise is less sensitive to the relative intensity of an emission spectrum than an absorption spectrum (see Section 3.1.2), relaxing the requirements on intensity matching: such an approach may therefore overcome some of the complexity of combined-beam observations and may even be practical for a multi-object instrument.

Another intriguing question is whether the interferometer comb itself could be used as a fiducial reference instead of iodine or ThAr. Changes in the interferometer delay will shift the phase of the comb, and so it can in principle track instrument drift, provided the comb and star signals can be adequately separated. The problem lies in the symmetry of the comb: as a simple example, if the image on the detector were to drift in a direction exactly parallel to the comb, the stellar fringes would appear to shift in phase and in the dispersion direction, and yet the comb would appear not to have changed at all, leading to the incorrect conclusion that the shift is wholly intrinsic to the star. If the image on the detector can reliably be stabilized to sufficient accuracy in either the slit or the dispersion direction (or both), then there would be sufficient information to break the degeneracy between stellar and instrument shift, and the intrinsic RV could be measured. This would be a big step forward, allowing simultaneous common-beam calibration with neither flux loss (as in iodine absorption) nor photon noise addition (as in ThAr superposition), and obviating the need for any reference spectrum at all. (The USNO dFTS instrument (Hajian et al. 2007), with its lack of dependence on simultaneous in-beam calibration, is somewhat similar in this respect, although a precise metrology system is needed to measure the varying interferometer delay.) As pointed out by our anonymous referee, the degeneracy could conceivably be broken given a sufficiently large spectral bandpass: the wavelength dependence of the comb frequency (see, e.g., Figure 3) would allow for the measurement of the image shift in the dispersion direction. The large bandpass, however, would need to be balanced with the requirement that the comb be resolved well enough to be measurable, which may be hard with standard CCD detector sizes unless longer wavelengths are used (since longer wavelengths exhibit a lower comb density in the dispersion direction).

Finally, if instrument stability can be controlled well enough, simply running parallel reference spectra alongside the stellar spectra, or alternatively, bracketing stellar exposures in time with reference exposures, can provide another solution: this has the twofold benefit of vastly simplifying the data analysis and eliminating the significant throughput loss (∼30%–50%) due to insertion of an iodine cell into the beam path. This is the current method of choice for the MARVELS survey, and is also currently employed by the KPNO ET. The MARVELS/Keck ET instrument is pressure stabilized, and thermally controlled to the few-mK level, allowing for very good instrument stability. Although not as precise as simultaneous common path calibration, the results are adequate for the moderate-precision large-scale survey for which the Keck ET is intended. On-sky results with the Keck ET show that this approach is feasible, and exposure bracketing is to be employed in the full survey.

4.4. The Technique in Practice

Beginning with the confirmation of 51 Peg b, and with the later discovery of HD 101195 b, the ET instruments have convincingly demonstrated the capacity of dispersed fixed-delay interferometry for exoplanet detection and discovery (van Eyken et al. 2004a; Ge et al. 2006). Even in the presence of the addition-approximation error, both the single-object ET at KPNO and the multi-object Keck/MARVELS ET at APO have been able to routinely uncover the RV signals of known exoplanets. The early KPNO ET, using in-beam iodine, demonstrated photon-limited precision at the 2–3 m s^{-1} level with bright reference stars on the very short term (see earlier, Figure 4). Figure 11 shows observations of η Cas, an RV-stable star, using the same instrument over a longer period of several months, with an rms of 10.8 m s^{-1} (compared to a mean photon limit of 5.6 m s^{-1}). Evidently in this case, the addition approximation error due to the iodine was not too extreme. For comparison, typical rms measurements on bright reference stars were on the order of 8–10 m s^{-1} over typical observing runs of ∼1 week, where

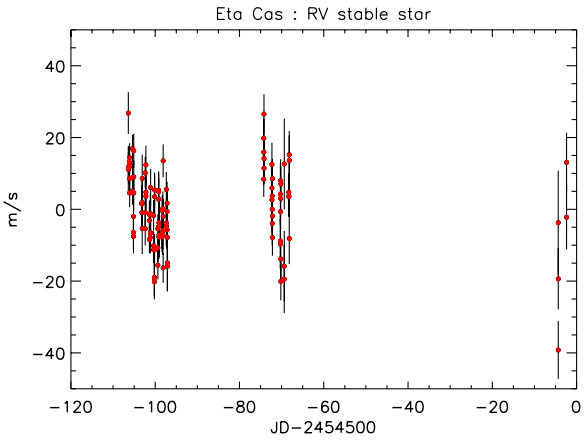

Figure 11. Differential RV measurements of η Cas, an RV stable star, using the single-object KPNO ET. The rms scatter is 10.8 m s^{-1}; error bars indicate the size of the photon error (mean 5.6 m s^{-1}), and do not include correlated systematic errors.

(A color version of this figure is available in the online journal.)

the addition approximation error would normally be quite small (and to some extent absorbed in determination of the phase-to-velocity scale, Γ).

In anticipation of the upcoming MARVELS survey, the Keck instrument saw a major upgrade in 2008, with a more stable mechanical design, pressure stabilization, and extremely precise thermal control, rendering the instrument stable enough to make exposure bracketing with tungsten-illuminated iodine reference spectra feasible. As a result, the addition approximation issue is eliminated and throughput substantially increased (albeit at the expense of some loss of precision due to the separated target and fiducial light paths). The baseline requirements for the MARVELS survey with this approach call for rms errors of 14 m s^{-1} and 35 m s^{-1} at $V = 8$ mag and $V = 12$ mag, respectively, with corresponding photon error components of 3.5 m s^{-1} and 21.5 m s^{-1} (Ge et al. 2009). HD 9407 (stable, $V = 6.6$ mag) shows an rms of 11.3 m s^{-1} over four months, fairly typical for stars at this brightest end of the target range; current typical performance shows an rms of 15 m s^{-1} at $V = 8$ mag, and 42 m s^{-1} at $V = 12$ mag.

The KPNO ET is currently being upgraded, and in light of the addition approximation error, observations are now also taken in an iodine bracketing mode, with no simultaneous calibration. Further details and results from both instruments can be found in van Eyken et al. (2004a, 2004b), Ge et al. (2006), Mahadevan (2006), van Eyken (2007), Mahadevan et al. (2008a, 2008b), and Ge et al. (2009). Such precisions are adequate for finding planets with minimum masses ($M \sin i$) of order 1 M_J or more in few-day orbits (i.e., hot Jupiters) down to $V = 12$. They are also more than adequate for uncovering stellar binary and brown dwarf companions.

We have presented here an overview of a mathematical basis for understanding DFDI data for precision RV measurements, and discussed analytical approaches to some of the error sources that would affect any implementation of the technique. The formulae derived should prove useful for interpreting the data from any future implementations of such instruments. As the ET instruments' overall precision and reliability continues to improve, it is our hope that the DFDI technique will be able to make a significant contribution to the known extrasolar planet sample over the coming years.

The multiple-object ET instrument was supported by the W. M. Keck Foundation, NSF with grant AST-0705139, NASA with grant NNX07AP14G, the SDSS-III program, and the University of Florida. The development of the single-object ET was supported by NSF with grant AST-0451407, NOAO, and the Pennsylvania State University.

J.vE. and S.M. gratefully acknowledge support from the JPL Michelson Fellowship program funded by NASA, and from Kitt Peak National Observatory for travel support for many nights of observing at the 2.1 m telescope. J.vE. also gratefully acknowledges support from the fellowship provided by the Pennsylvania State University, and from the SPIE scholarship program. This work has made use of the IDL Astronomy User's Library (Landsman 1993),[12] and Craig Markwardt's IDL library.[13]

Funding for SDSS-II has been provided by the Alfred P. Sloan Foundation, the Participating Institutions, and the National Science Foundation.

SDSS-III is managed by the Astrophysical Research Consortium for the Participating Institutions. The Participating Institutions are the University of Cambridge, Case Western Reserve University, University of Portsmouth, Johns Hopkins University, Princeton University, the Korean Scientist Group, the Max-Planck-Institute for Astrophysik, New Mexico State University, Ohio State University, University of Pittsburgh, Brazilian RIO Group, German Participation Group, New York University, University of California-Santa Clara, University of Florida, and the University of Washington.

The SDSS-III Web Site is: http://www.sdss3.org

The Center for Exoplanets and Habitable Worlds is supported by the Pennsylvania State University, the Eberly College of Science, and the Pennsylvania Space Grant Consortium.

We gratefully acknowledge our anonymous referee's input which helped substantially improve this paper. J.vE. thanks Peter Plavchan for much useful discussion of the addition approximation error, Dimitri Veras for proofreading of early versions, and Justin Crepp for his helpful suggestions.

Facilities: KPNO:2.1m (ET), Sloan (Keck ET), HET

APPENDIX A

THE SPECTROGRAPH RESPONSE FUNCTION AND THE LSF

The response function $w_j(\lambda)$ due to the spectrograph optics is very closely related to the instrument LSF. As defined for the purposes of this paper, the spectrograph response function specifies the respective instrumental throughputs for the finite range of wavelengths, λ, falling at a given position in the dispersion direction, $x = j$, on the detector, corresponding to a spatially infinitesimally narrow channel in the spectrum. By contrast, the LSF specifies the flux distribution on the detector as a function of spatial position in the dispersion direction due to a single monochromatic wavelength of light. The response function at a particular position is therefore determined by the way the LSFs from all the different wavelengths overlap at that position.

If we assume the LSF is approximately identical in form at closely separated channels x on the detector, where x represents the pixel position in the dispersion direction (not necessarily integer), then we can define the LSF as $L(x, x_0(\lambda_0)) = L_t(x -$

[12] See also http://idlastro.gsfc.nasa.gov/

[13] http://cow.physics.wisc.edu/~craigm/idl/idl.html

$x_0(\lambda_0)$) where L represents the normalized envelope of flux spread across pixels x on the detector due to monochromatic light of wavelength λ_0, centered at position x_0. L is simply a shifted version of $L_t(x)$, which represents a template of the LSF centered at $x = 0$. In general, $x(\lambda)$ represents the wavelength calibration mapping wavelength to detector position.

The response function at an infinitesimally wide position on the detector, w, is given by writing the contribution from each overlapping LSF at that position. The contribution from wavelength λ_0 at position x_1 is given by $w(\lambda_0, x_1) = L(x_1, x_0(\lambda_0)) = L_t(x_1 - x_0(\lambda_0))$. Therefore, as a continuous function of general wavelength λ, we can write the response function at position x_1 as

$$w(\lambda, x_1) = L_t(x_1 - x(\lambda)). \tag{A1}$$

We see that this is really just the LSF reversed (since the x term is now negative).

We can now extend this to the total contribution across an entire pixel at position $x = j$ where j is now an integer representing pixel number. Let $t_j(x')$ represent the pixel response function, describing the normalized throughput of the pixel across its width as a function of x'. Then we can write $w(\lambda, x')t_j(x')\,dx' = L_t(x' - x(\lambda))t_j(x')\,dx'$. Summing over all x', we have the full response function W_j for pixel column j, given by

$$W_j(\lambda) = \int L_t(x' - x(\lambda))t_j(x')\,dx', \tag{A2}$$

i.e., essentially a convolution of the response function with the pixel response function. To the extent that the width of the pixel is narrow compared to the LSF (i.e., that the image is well oversampled), then to a reasonable approximation, t_j is close to a delta function, $W \approx w$, and the instrument response function at position x is approximately just the reversed LSF. Analogous arguments can be followed in wavenumber (κ) space instead of wavelength space, simply replacing λ with κ to obtain the same exactly the same results as a function of κ.

APPENDIX B

FRINGE FORMATION: AN ALTERNATIVE VIEWPOINT

We can view the formation of the fringes as given by Equation (8) in another way. Beginning again with Equation (1) for the flux at a given channel, j, as a function of delay d, and again substituting Q, we can write

$$\begin{aligned} I_j(d) &= \int Q(\kappa)\,\Re\{1 + e^{-i2\pi\kappa d}\}\,d\kappa \\ &= \int P(\kappa)w_j(\kappa)[1 + \cos(2\pi\kappa d)]d\kappa, \end{aligned} \tag{B1}$$

where again the spectrum within the channel is given by $Q(\kappa) = P(\kappa)w_j(\kappa)$, with $P(\kappa)$ being the full spectrum entering the instrument, and $w_j(\kappa)$ being the spectrograph response function for channel j.

If we assume that the spectrograph response function is uniform across the whole spectrum (i.e., for all j), then we can express it as a wavenumber-shifted version of a global "template" spectrograph response function, w_t (which is centered at $\kappa = 0$), shifted so that its center is at the central wavenumber of the channel in question, κ_j. From Appendix A, we know that the spectrograph response function is just the reverse of the LSF, so we can write

$$w_j = w_t(\kappa - \kappa_j) = L_t(\kappa_j - \kappa), \tag{B2}$$

where L_t represents a global template LSF, also centered at $\kappa = 0$. If we furthermore define $T(\kappa, d) \equiv 1 + \cos(2\pi\kappa d)$, we can therefore rewrite Equation (B1) as

$$I_j(d) = \int P(\kappa)T(\kappa, d)L_t(\kappa_j - \kappa)d\kappa. \tag{B3}$$

T can be thought of as the interferometer transmission function, equivalent to the interferogram that would be obtained for pure white light and an infinite resolution spectrograph (exactly as in Equation (12)). Equation (B3) can be identified as a convolution over the variable κ:

$$I_j(d, \kappa_j) = [P(\kappa)\,T(\kappa, d)] \otimes L_t(\kappa), \tag{B4}$$

where the convolution is evaluated at wavenumber κ_j.

In other words, we have simply the input spectrum multiplied with the interferometer transmission function, and then convolved with the LSF due to the spectrograph. Thinking in two dimensions, to match the wide-slit format of the actual ET spectra, we can replace the LSF with its two-dimensional equivalent, the instrument point spread function (PSF). Exactly the same results can be derived in frequency space, simply by substituting frequency ν for κ and time delay τ for d.

This way of looking at fringe formation is the approach used by Erskine (2003) and followed by Mahadevan (2006), and can conveniently be employed to quickly produce simulated DFDI spectra (although with the caveat that it assumes a uniform LSF, which in practice is unlikely to be very realistic).

APPENDIX C

DIVISION-OF-MEANS APPROXIMATION

In Section 3.2, we make an approximation regarding the magnitude of velocity errors resulting from a contaminant spectrum, where we state that the error in velocity is approximately equal to the flux ratio of the contaminant to the true source spectrum multiplied by the velocity difference between the two spectra (Equation (56)). Namely, we assume that $\langle F_c/F_s\rangle \approx \langle F_c\rangle/\langle F_s\rangle$ (we will use $\langle\cdots\rangle$ to represent the mean here for notational convenience). The same is assumed several times in the same section (Equations (57) and (59)). This approximation holds true provided that the fractional variation in the power spectrum in the denominator with wavelength is predominantly relatively small. We also make the same approximation regarding the division of mean visibilities in Sections 3.3.2 and 3.3.3 (Equations (60) and (64)). Here we show the validity of this approximation.

Consider two arbitrary functions $A(x)$ and $B(x)$, which have fractionally relatively small variations about their means so that we can define two corresponding functions, $a(x)$ and $b(x)$ such that

$$A(x) \equiv \langle A\rangle(1 + a(x)); \quad B(x) \equiv \langle B\rangle(1 + b(x)), \tag{C1}$$

where $a, b \ll 1$ for all x. Using the binomial expansion, we can write

$$\begin{aligned} \left\langle \frac{A}{B} \right\rangle &= \left\langle \frac{\langle A\rangle(1+a)}{\langle B\rangle(1+b)} \right\rangle = \frac{\langle A\rangle}{\langle B\rangle}\left\langle \frac{1+a}{1+b} \right\rangle \\ &= \frac{\langle A\rangle}{\langle B\rangle}\langle(1 + a)(1 - b + b^2 - b^3 + \cdots)\rangle \\ &= \frac{\langle A\rangle}{\langle B\rangle}\langle 1 - b + b^2 - b^3 + \cdots + a - ab + ab^2 - ab^3 + \cdots\rangle \\ &\approx \frac{\langle A\rangle}{\langle B\rangle}[1 + \langle b^2\rangle - \langle ab\rangle], \end{aligned} \tag{C2}$$

where we have neglected terms of order b^3 and ab^2 and smaller, and where we can also drop the terms $\langle a \rangle$ and $\langle b \rangle$, which must equal zero according to the definitions of a and b.

In general, $\langle ab \rangle \rightarrow 0$ if the functions a and b (and hence A and B) are uncorrelated. In the limit where the two functions are completely correlated (i.e., identical), then $\langle ab \rangle \rightarrow \langle b^2 \rangle$, and the $\langle ab \rangle$ and $\langle b^2 \rangle$ terms cancel, so that $\langle A/B \rangle \rightarrow \langle A \rangle / \langle B \rangle$. In the cases we are interested in, it is generally unlikely that $\langle ab \rangle \ll 0$ (anticorrelation), or that $\langle ab \rangle \gg \langle b^2 \rangle$. Therefore, we can reasonably take $\langle b^2 \rangle$ as an estimate of the fractional error in the division approximation. Conveniently, from the definition of b, $\langle b^2 \rangle$ turns out to be equal to the square of the normalized standard deviation, σ_B, of the function B:

$$\langle b^2 \rangle = \frac{\langle (B - \langle B \rangle)^2 \rangle}{\langle B \rangle^2} = \left(\frac{\sigma_B}{\langle B \rangle} \right)^2 . \quad \text{(C3)}$$

Hence for functions with small fractional deviations from their respective means, the mean of the quotient is approximately equal to the quotient of the means, and $(\sigma_B / \langle B \rangle)^2$ gives an estimate of the fractional error in the approximation.

Tests with stellar spectra show the approximation works quite well, both at ET-like resolutions and with very high resolution synthetic spectra. Taking as an example $R \sim 5000$ spectra from the KPNO ET of 36 UMa (F8V) and τ Cet (G8V) (obtained by binning the fringing spectra along the slit direction), we find $\sigma_{\tau \mathrm{Cet}} / \langle F_{\tau \mathrm{Cet}} \rangle = 0.25$, giving an estimated error of 6% due to the approximation. In practice, we find the ratio of $\langle F_{36\mathrm{UMa}} \rangle / \langle F_{\tau \mathrm{Cet}} \rangle$ to $\langle F_{36\mathrm{UMa}} / F_{\tau \mathrm{Cet}} \rangle$ to be 0.980, i.e., a 2% difference. For an *emission* spectrum in the denominator, such as ThAr, the approximation will not hold well as there are significant regions of near-zero flux. However, it is unlikely that one would be interested in considering some contaminant spectrum against a primary emission spectrum source. Conceivably one might be interested in considering the effects of contamination *from* an emission source—e.g., from stray fluorescent lighting leakage, sky emission, or leakage from an reference lamp, but in this case the emission spectrum would be in the numerator: a stellar spectrum will always be the function in the denominator, and so the approximation should still hold.

The second case where the approximation is employed is in considering visibility ratios, as in estimating the velocity error due to the reference whirl addition approximation, or estimating the effect of residual interferometer comb (Equations (60) and (64)). In both cases here the function in the denominator is absolute visibility as a function of wavelength, $\alpha(\lambda)$, for reference-multiplied stellar data (since the comb and cross-talk terms both appear in the formula for the combined star/reference data, Equation (22)). Taking KPNO spectra as an example, the normalized variance of the combined star/iodine data tends to be around $(\sigma_\alpha / \langle \alpha \rangle)^2 \approx 0.32$, in other words giving an estimated error in the division approximation of around 30% for both comb and cross-talk error sources—not as precise as the approximation for contaminating spectra, but still useful for an order-of-magnitude error. In neither of these cases do we expect any correlation between the data visibility function in the denominator and the comb or cross-talk visibility function in the numerator, so the $\langle ab \rangle$ term should be small.

Where there is concern over the assumptions made above (e.g., where the normalized variance of the denominator, $(\sigma_B / \langle B \rangle)^2$ is not small—which would, for example, be the case were the denominator to represent visibilities of a pure star spectrum, where the visibility distribution peaks at very low values), then the approximation derived here is not appropriate, and instead it is necessary to calculate $\langle F_c / F_s \rangle$ directly. Often this is in fact entirely practical; however the approximation can generally be used to give a very quick and convenient first-order estimate of contamination errors.

REFERENCES

Armitage, P. J. 2007, ApJ, 665, 1381
Baranne, A., et al. 1996, A&AS, 119, 373
Barker, L. M., & Hollenbach, R. E. 1972, J. Appl. Phys., 43, 4669
Barker, L. M., & Schuler, K. W. 1974, J. Appl. Phys., 45, 3692
Beckers, J. M., & Brown, T. M. 1978, in Proc. JOSO Workshop, Future Solar Optical Observations Needs and Constraints, ed. G. Godoli, G. Noci, & A. Righini (Firenze: Baccini e Chiappi), 189
Behr, B. B., Hajian, A. R., Cenko, A. T., Murison, M., McMillan, R. S., Hindsley, R., & Meade, J. 2009, ApJ, 705, 543
Butler, R. P., Marcy, G. W., Williams, E., McCarthy, C., Dosanjh, P., & Vogt, S. S. 1996, PASP, 108, 500
Campbell, B., & Walker, G. A. H. 1979, PASP, 91, 540
Connes, P. 1985, Ap&SS, 110, 211
da Silva, R., et al. 2006, A&A, 446, 717
Douglas, N. G. 1997, PASP, 109, 151
Edelstein, J., Erskine, D. J., Lloyd, J., Herter, T., Marckwordt, M., & Feuerstein, M. 2006, Proc. SPIE, 6269, 62691E
Edser, E., & Butler, C. P. 1898, Philos. Mag., 46, 207
Erskine, D. J. 2003, PASP, 115, 255
Erskine, D. J., & Edelstein, J. 2004, Proc. SPIE, 5492, 190
Erskine, D. J., Edelstein, J., Feuerstein, W. M., & Welsh, B. 2003, ApJ, 592, L103
Erskine, D. J., & Ge, J. 2000, in ASP Conf. Ser. 195, Imaging the Universe in Three Dimensions, ed. W. van Breugel & J. Bland-Hawthorn (San Francisco, CA: ASP), 501
Fischer, D. A., & Valenti, J. 2005, ApJ, 622, 1102
Forrest, A. K., & Ring, J. 1978, in Proc. 4th International Colloquium on Astrophysics, High Resolution Spectrometry, ed. M. Hack (Trieste: Osservatorio astronomico di Trieste), 462
Frandsen, S., Douglas, N. G., & Butcher, H. R. 1993, A&A, 279, 310
Ge, J. 2002, ApJ, 571, L165
Ge, J., Eisenstein, D., & Gaudi, B. S. 2009, Astro2010 Astronomy and Astrophysics Decadal Survey Science White Paper, 86 (arXiv:0903.0181)
Ge, J., Erskine, D. J., & Rushford, M. 2002, PASP, 114, 1016
Ge, J., Mahadevan, S., van Eyken, J., Dewitt, C., & Shaklan, S. 2003a, in ASP Conf. Ser. 294, Scientific Frontiers in Research on Extrasolar Planets, ed. D. Deming, S. Seager (San Francisco, CA: ASP), 573
Ge, J., van Eyken, J. C., Mahadevan, S., DeWitt, C., Ramsey, L. W., Shaklan, S. B., & Pan, X. 2003b, Proc. SPIE, 4838, 503
Ge, J., et al. 2006, ApJ, 648, 683
Geake, J. E., Ring, J., & Woolf, N. J. 1959, MNRAS, 119, 616
Goodman, J. W. 1985, Statistical Optics (New York: Wiley)
Gorskii, S. M., & Lebedev, V. P. 1977, Izv. Krym. Astrofizika Obs., 57, 228
Griffin, R., & Griffin, R. 1973, MNRAS, 162, 243
Hajian, A. R., et al. 2007, ApJ, 661, 616
Harlander, J., Reynolds, R. J., & Roesler, F. L. 1992, ApJ, 396, 730
Harvey, J., & The GONG Instrument Team 1995, in ASP Conf. Ser. 76, GONG 1994. Helio- and Astro-Seismology from the Earth and Space, ed. R. K. Ulrich, E. J. Rhodes, & Jr., W. Dappen (San Francisco, CA: ASP), 432
Hilliard, R. L., & Shepherd, G. G. 1966, J. Opt. Soc. Am., 56, 362
Jacquinot, P. 1960, Rep. Prog. Phys., 23, 267
Johnson, J. A., et al. 2006, ApJ, 647, 600
Kane, S. R., Collier Cameron, A., Horne, K., James, D., Lister, T. A., Pollacco, D. L., Street, R. A., & Tsapras, Y. 2004, MNRAS, 353, 689
Konacki, M., Muterspaugh, M. W., Kulkarni, S. R., & Hełminiak, K. G. 2009, ApJ, 704, 513
Landsman, W. B. 1993, in ASP Conf. Ser. 52, Astronomical Data Analysis Software and Systems II, ed. R. J. Hanisch, R. J. V. Brissenden, & J. Barnes (San Francisco, CA: ASP), 246
Lawson, P. R. 2000, in Principles of Long Baseline Stellar Interferometry, ed. P. R. Lawson (Pasadena, CA: NASA JPL), 113
Loeillet, B., et al. 2008, A&A, 479, 865
Mahadevan, S. 2006, PhD thesis, Univ. of Florida
Mahadevan, S., Ge, J., Fleming, S. W., Wan, X., DeWitt, C., van Eyken, J. C., & McDavitt, D. 2008a, PASP, 120, 1001
Mahadevan, S., Ge, J., van Eyken, J. C., DeWitt, C., & Shaklan, S. B. 2003, Proc. SPIE, 5170, 184

Mahadevan, S., van Eyken, J., Ge, J., DeWitt, C., Fleming, S. W., Cohen, R., Crepp, J., & Vanden Heuvel, A. 2008b, ApJ, 678, 1505
Mayor, M., & Queloz, D. 1995, Nature, 378, 355
McMillan, R. S., Moore, T. L., Perry, M. L., & Smith, P. H. 1993, ApJ, 403, 801
McMillan, R. S., Moore, T. L., Perry, M. L., & Smith, P. H. 1994, Ap&SS, 212, 271
Michelson, A. A. 1903, Light Waves and their Uses (Chicago, IL: Univ. of Chicago Press)
Mosser, B., Maillard, J.-P., & Bouchy, F. 2003, PASP, 115, 990
Pepe, F., et al. 2005, Messenger, 120, 22
Shepherd, G. G., et al. 1985, Appl. Opt., 24, 1571
Szentgyorgyi, A. H., & Furész, G. 2007, RevMexAA Conf. Ser., 28, 129
Udry, S., Fischer, D., & Queloz, D. 2007, in Protostars and Planets V, ed. B. Reipurth, D. Jewitt, & K. Keil (Tucson, AZ: Univ. Arizona Press), 685
van Eyken, J. C. 2007, PhD thesis, Univ. of Florida
van Eyken, J. C., Ge, J., Mahadevan, S., & DeWitt, C. 2004a, ApJ, 600, L79
van Eyken, J. C., Ge, J., Mahadevan, S., DeWitt, C., Friedman, J., Finnerty, P., Ren, D., & Zugger, M. 2004b, Proc. SPIE, 5492, 445
van Eyken, J. C., Ge, J., Mahadevan, S., DeWitt, C., & Ren, D. 2003, Proc. SPIE, 5170, 250
Vogt, S. S., Marcy, G. W., Butler, R. P., & Apps, K. 2000, ApJ, 536, 902